



Maria João Portela de Sá Pereira **Preparação e estudo de filmes Ni-Mn-Ga depositados por sputtering**

Preparation and study of Ni-Mn-Ga films prepared by sputtering



Maria João Portela de Sá Pereira **Preparação e estudo de filmes Ni-Mn-Ga depositados por sputtering**

Preparation and study of Ni-Mn-Ga films prepared by sputtering

Dissertação apresentada à Universidade de Aveiro para cumprimento dos requisitos necessários à obtenção do grau de Mestre em Ciência e Engenharia de Materiais, realizada sob a orientação científica do Professor Doutor Vítor Amaral, Professor Catedrático do Departamento de Física da Universidade de Aveiro.

Apoio financeiro no âmbito do programa FP6
projecto "Multiceral" No. NMP3-CT-2006-032616.

o júri

presidente

Professor Doutor Nikolai Andreevich Sobolev
professor associado do Departamento de Física da Universidade de Aveiro

Prof. Doutor João Pedro Esteves de Araújo
professor auxiliar da Faculdade de Ciências da Universidade do Porto

Professor Doutor Vítor Brás de Sequeira Amaral
professor catedrático do Departamento de Física da Universidade de Aveiro

Professor Doutor Armando António Cardoso dos Santos Lourenço
professor auxiliar do Departamento de Física da Universidade de Aveiro

agradecimentos

First of all, I would like to thank my supervisor, Prof. Dr. Vítor Amaral, for his constant guidance, assistance and support. I would also like to thank my co-supervisor, Prof. Dr. Armando Lourenço, for all the knowledge he shared during the process of sample fabrication.

I would also like to thank Prof. Dr. Sobolev and his student Nuno Santos for allowing me to include their FMR results on this thesis, as well as Prof. Dr. Pedro Tavares for providing the equipment to perform SEM and EDS measurements.

I would like to especially thank PhD student Fábio Figueiras for his precious help in preparing this thesis and PhD student Marco Peres who performed the XRD measurements, as well as Post Doc. Soma Das for her help and cooperation.

Finally, I would like to thank my boyfriend Bruno for his love, endless patience and invaluable help in every crucial moment, and my sister Ana and my brother António for their everlasting cooperation, friendship and for being the best brother and sister that anyone could ever wish for. I would also like to thank my parents for their love, for providing for my education, and for always encouraging me to live up to my potential while keeping my feet on the ground.

palavras-chave

ligas ferromagnéticas com memórias de forma, Ni-Mn-Ga, filmes finos, pulverização catódica

resumo

Na última década as ligas ferromagnéticas com memórias de forma têm atraído uma atenção crescente devido à sua importância tecnológica e às suas interessantes propriedades físicas. Em particular, o estudo das propriedades de ligas ferromagnéticas com memórias de forma de Ni₂MnGa sob a forma de filmes finos depositados por pulverização catódica por radiofrequência suscita um interesse especial por constituir uma possibilidade de aplicação em micro e nanosistemas. As suas propriedades dependem da estrutura dos filmes finos, que se desenvolve durante o processo de deposição. Neste estudo foram depositados filmes finos de Ni₂MnGa em cinco substratos (vidro, Al₂O₃, Si, SrTiO₃ e MgO) com diferentes orientações, sob diferentes condições de pulverização catódica por radiofrequência, e as suas composições, estruturas e propriedades magnéticas foram analisadas através dos métodos de EDS, XRD e VSM, respectivamente. Concluímos que a maioria das amostras apresentam magnetizações de saturação da mesma ordem da magnetização de saturação do material "bulk" com a mesma composição. O comportamento ferromagnético dos filmes finos em estudo é estável até 300K. As medidas de FMR efectuadas revelaram uma temperatura de Curie aproximadamente igual a 350K, o que confirma a qualidade dos filmes finos, dado que a temperatura de Curie do material "bulk" é cerca de 360K. A deposição a baixa temperatura (cerca de 400 °C) foi, pois, efectuada com sucesso.

keywords

ferromagnetic shape memory alloys, Ni-Mn-Ga, thin films, sputtering

abstract

In the last decade ferromagnetic shape memory alloys (FSMAs) have been attracting increasing attention because of their technological importance and interesting physical properties. In particular, the study of the properties of Ni₂MnGa FSMAs as deposited in thin films by r.f. sputtering raises a special interest because of their prospective application to micro and nanosystems. These properties strongly depend on the thin films' structures which are developed during the process of sputtering deposition. In this study Ni₂MnGa thin films deposited on five substrates (glass, Al₂O₃, Si, SrTiO₃ and MgO) with different orientations, under different sputtering conditions had their compositional, structural and magnetic properties studied by EDS, XRD and VSM, respectively. We concluded that most of the samples show saturation magnetisations of the same order of the saturation magnetisation of the bulk material of the same composition. The ferromagnetic behaviour of the thin films under study is stable up to 300K. FMR measurements revealed a Curie temperature (T_C) of approx. 350 K, which confirms the thin films' quality, since bulk T_C for the same composition is about 360K. The low temperature deposition (at around 400 °C) was thus successfully achieved.

CONTENTS

1. Sputtering	3
1.1. Introduction	3
1.2. Sputtering mechanism	5
1.2.1. Sputter yield	7
1.2.2. Sputtering rates	10
1.3. Plasmas and gaseous discharges	11
1.3.1. Plasmas	11
1.3.2. Glow discharges for sputtering	13
1.4. Sputtering techniques	15
1.4.1. DC sputtering	15
1.4.2. RF magnetron sputtering	19
1.4.2.1. RF sputtering	19
1.4.2.2. Magnetron sputtering	20
1.5. Sputtering versus evaporation	22
2. Shape memory alloys: Ni ₂ MnGa	24
3. Experimental Details	29
3.1. Sample fabrication	29
3.2. Characterisation	32
3.2.1. EDS	32
3.2.2. SEM	32
3.2.3. XRD and X-ray reflectivity	32
3.2.4. VSM	33
4. Results and discussion	34
4.1. EDS measurements	34
4.2. SEM measurements	36
4.3. X-ray measurements	40
4.3.1. X-ray reflectometry measurements	40
4.3.2. XRD measurements	43
4.4. VSM measurements	46

4.5. FMR measurements	54
5. Conclusions and future studies	56
5.1. Conclusions	56
5.2. Future studies	57
6. Bibliography	58

1. SPUTTERING

1.1. INTRODUCTION

Sputter deposition has become one of the most used processes of physical vapour deposition. The sputtering process is currently well understood.

A broad definition of sputtering is given by Sigmund (1993), who describes it as: “*the erosion of material surfaces by particle impact*”. Sigmund also says that “*Sputtering is a phenomenon on the atomic scale. By this is meant that one can identify an individual sputter event, i.e., the emission of a number of atoms or molecules from a material surface initiated by a single bombarding particle.*”

The sputtering process was discovered around 1852 by W. R. Grove, when he was studying neon lights. He noted the formation of a dark colour inside the tube adjacent to the electrode which he then supposed to be due to a transference of material from the electrode to the inside wall of the tube. This was, in fact, the first time a sputtering event was acknowledged. The equipment used by Grover in these experiments is shown on Fig. 1.1.

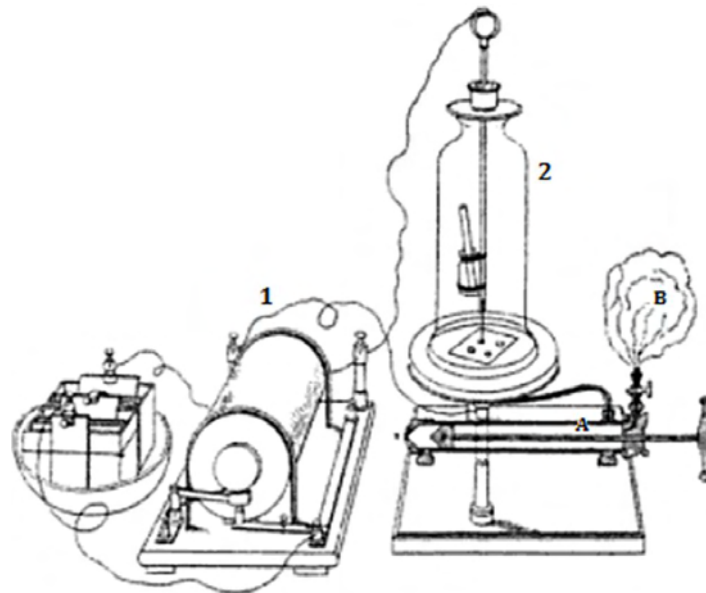


Fig. 1.1 Drawing of the apparatus used by Grove in his first sputtering studies. 1 is the coil apparatus using for generating a high voltage; the contact breaker is shown in front. 2 is the vacuum vessel containing an electrode and a polished silver plate, on which deposits were observed. The air pump used to evacuate the vessel is (A), and a bladder (B) contained a gas sample used for studies of discharges in different gases.[6]

Despite this early beginning, the sputtering technique would only know a relevant development in the 1920's with the work performed by Irwin Langmuir, which laid the foundation for modern plasma physics and gave us a deeper insight on the gas discharge environment in which sputtering operates. With the introduction of modern vacuum pumping technology, it became possible to use the process commercially, namely to deposit metal thin films used in the manufacturing of phonograph records [6].

The sputtering process operates on an atomic or molecular scale and consists on the ejection of atoms from an electrode surface (target) by momentum transfer from bombarding ions to surface atoms [4]. The momentum of the incident particle is transferred to the atoms on the surface of the target and this transfer of momentum might lead to the ejection of some of these atoms. Fig. 1.2 is a scheme of the events that occur in sputtering.

The energetic ions are obtained from a plasma discharge and are usually Argon ions. Other particles are known to cause sputtering such as electrons and photons. The reason why the incident particles are ions is because these particles need to be of atomic dimensions in order for the sputtering process to be efficient. Smaller particles are not able to carry enough momentum to perform the sputtering process adequately. At the same time, if the incident particle is too large it will be so massive that it will not be able to interact with individual atoms or molecules on the surface.

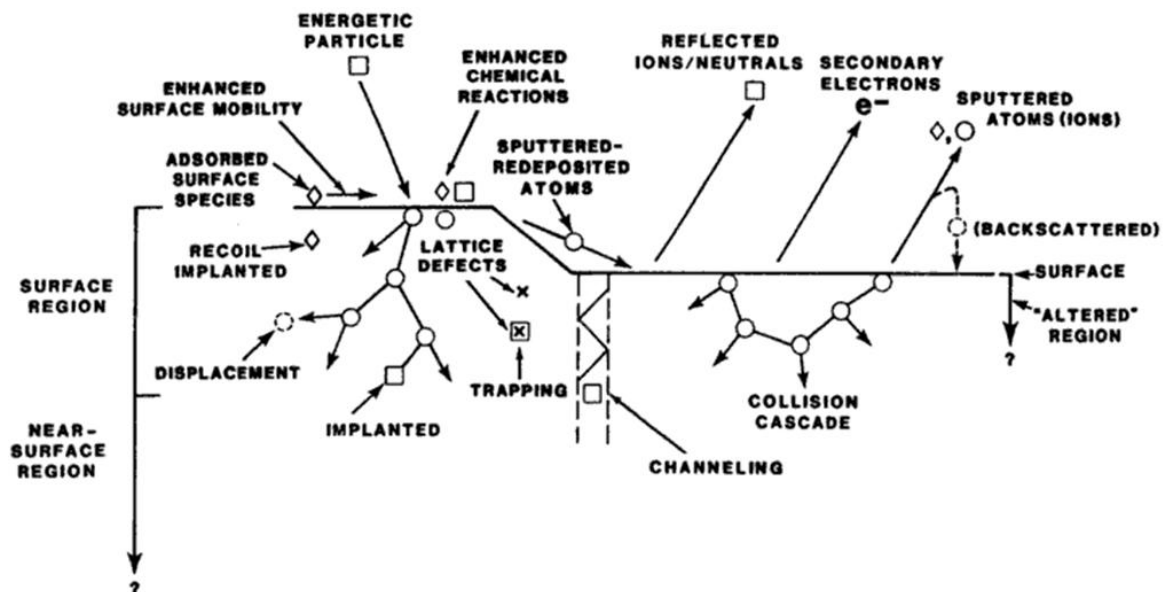


Fig. 1.2 Events occurring on a surface being bombarded with energetic atomic-sized particles [16]

The particles emitted are predominantly neutral atoms in the ground state [15]. However, the target might also emit ions and clusters. The atoms ejected from the target traverse a reduced pressure ambient and deposit on a substrate, forming a coating.

Fig. 1.3 also shows the sputtering event, focusing on the following events: acceleration of an ion across the cathode sheath; penetration of the target, resulting in a series of atomic collisions; backward ejection of one or more recoiling target atoms.

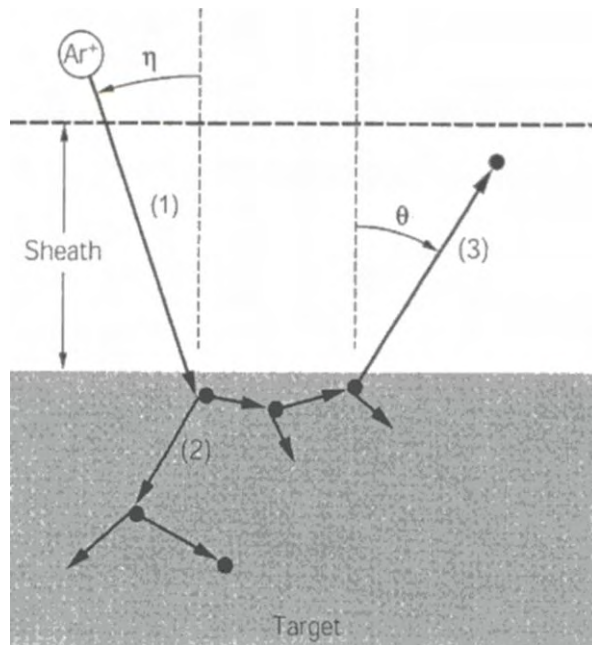


Fig. 1.3 Schematic representation of the sputtering process. η is the angle of incidence and θ is the emission angle. [5]

Of the many possible applications of the sputtering technique, the deposition of films is the one that is relevant for the present dissertation.

1.2. SPUTTERING MECHANISM

When ion impact causes a series of collision events on the target which lead to the ejection of an atom from the target material, it can be said that we are dealing with the event of sputtering. In this context, the process shown in Fig. 1.4 is more specifically called “collisional sputtering”.

Most of the literature that has been published on the subject indicates that sputtering is related to momentum transfer from energetic particles to the surface atoms of the target. Thus, it is common to use the “atomic pool” analogy to explain the phenomenon. In this analogy, the energetic particle (usually an ion) would be the cue ball, whereas the close-packed rack of atoms would be the billiard balls. The ion (cue ball) hits the surface atoms of the target (billiard balls) scattering some of these backward (in the direction of the “player”). Although “*forward*” sputtering can also occur (in the case of sputtering of very thin foils), this is rather a “*backward*” sputtering.

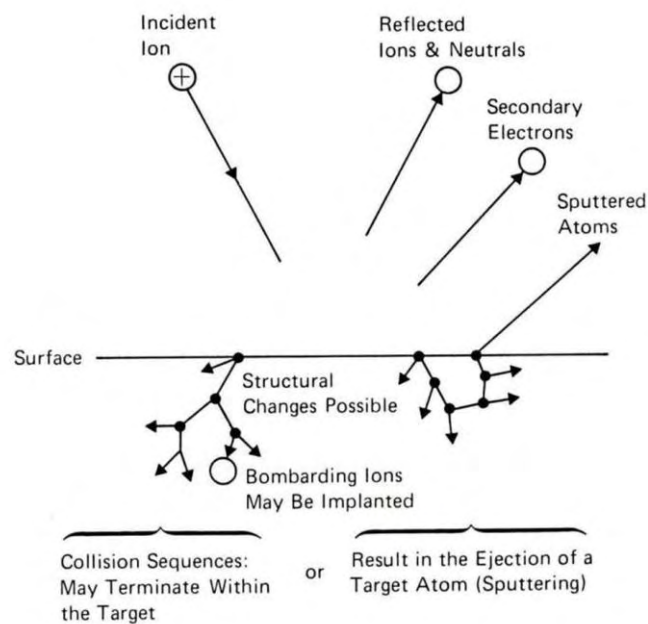


Fig. 1.4 *The Sputtering Process (Chapman 1980) [7]*

Sigmund described the mechanism of collisional sputtering in this way: “*The elementary event is an atomic collision cascade wherein the incident ion knocks atoms off their equilibrium sites in the target, thus causing these atoms to move through the material, to undergo further collisions, and eventually to cause the ejection of atoms through the target surface. The general consensus is that this sputtering mechanism is the most universal one, being active for ionic bombardment of all types of solids at appropriate ion energies.*”[3]

1.2.1. Sputter yield

The most fundamental parameter which characterizes the sputtering process is the “sputter yield” in the sense that it is a measure of the efficiency of the process. The sputter yield (S) is defined as the mean number of atoms or molecules ejected from the surface per incident particle (eq. 1.1). [2]

$$S = \frac{\textit{atoms removed}}{\textit{incident ions}} \quad (1.1)$$

The sputter yield will be influenced by the following factors: incident particle energy and mass, mass of target atoms, incident angles of particles, atomic crystallinity, crystal structure and orientation of the target surface and binding energy of atoms in the solid. On the other hand, the sputter yield is nearly independent of the temperature of the target [22][23][24][14].

- Sputter yield dependence on incident ion energy

Fig. 1.5 shows the dependence of the sputter yield on the energy of the incident ions.

At relatively low incident ion energies the sputtering yield is very low, because it is not possible to supply enough energy to break the atomic bonds of the surface atoms, which will make the sputtering effect not noticeable. The sputter yield then starts increasing with the incident ion energy until it reaches a maximum value.

In the case of Fig. 1.5, the maximum sputter yield is achieved for incident ion energies around 10^5 keV. Beyond this energy, the decrease of the sputtering yield is due to the deeper penetration of the ions in the target – ion implantation [14]. Particles travelling too deeply in the target will lead to deep-level collisions, which does not contribute to release surface atoms.

Thus, it is only at energies around 100 eV that sputtering will be accomplished successfully. In this case, sputter yield ranges from values around 0.1 to 5 for most materials, being that for the majority of the materials it takes values between 0.5 and 2.

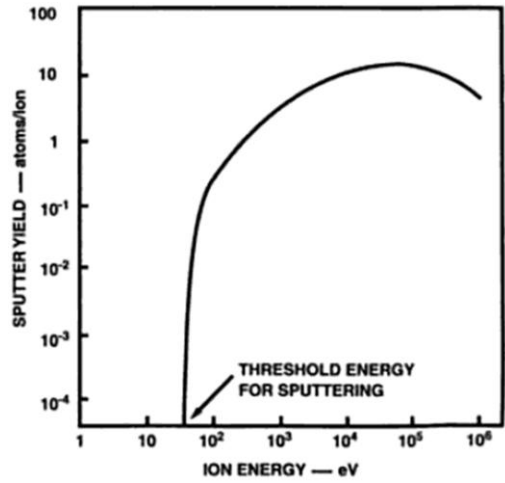


Fig.1.5 Sputter yield as a function of the incident ion energy [14]

- Sputter yield dependence on incident ion mass [26]

Fig. 1.6 shows the dependence of the sputter yield in the atomic number, Z , of the incident ions.

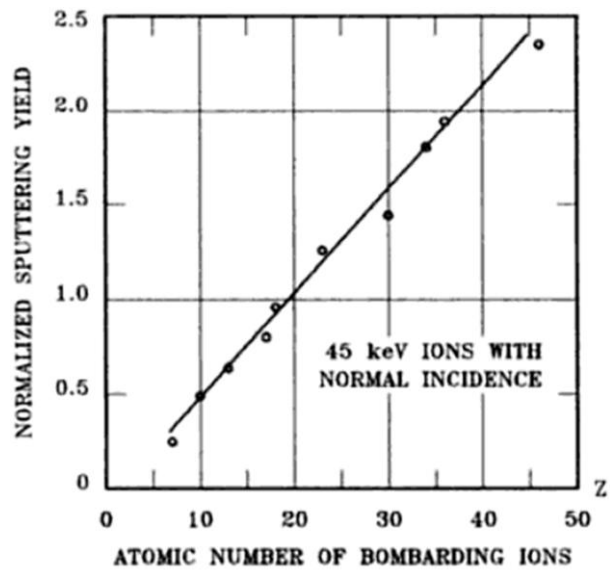


Fig. 1.6 Sputter yield of Si, normalized to Si sputter yield for Ar, vs. Z of bombarding ions

It can be observed that lighter incident ions will lead to lower values of sputter yield for the same energy and target material. H_2 and He ions, for instance, have very little sputter yield compared to N_2 and Ar ions accelerated through the same voltage.

- Sputter yield dependence on incident angle [26]

The incident angles of particles are defined as the angle formed by the trajectory of the ion with an imaginary line perpendicular to the target surface.

Fig. 1.7 shows a gradual increase of the sputter yield with the increasing angle of incidence until around 70°. After this value, the sputter yield decreases rapidly with the increasing angle.

This behaviour can be understood if we compare it to the behaviour of a stone being thrown at the water. If we throw the stone with an incident angle of 0°, the stone will dive directly into the water without much splashing.

However, as we increase the angle of incidence of the stone, the splash also increases progressively.

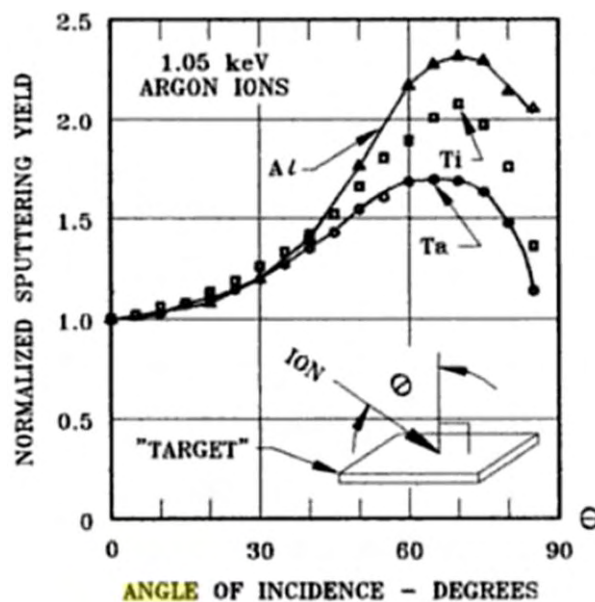


Fig. 1.7 Sputter yield versus incident angle of ions [26]

This behaviour is verified until values close to but smaller than 90°. In this case the stone does not break the surface of the water, making a very little splash. For angles even closer to 90°, the perturbation to the water will be smaller and smaller.

1.2.2. Sputtering Rates

The sputtering rate is determined by a group of different factors [27]:

- ✓ Gas pressure
- ✓ Current flowing in the discharge
- ✓ Type of gas (mass, energy and angle of incidence of the bombarding ions)
- ✓ Target material (mass, crystal orientation and temperature)

The pressure appears to be the most important of these aspects. It was found empirically that the sputtering rate varies inversely to the n^{th} power of the pressure (n is usually higher than 2 and can reach the value of 5) [27].

The current flowing in the discharge is almost as important as the pressure of the gas. In practice, the sputtering rate varies directly with the square or cube of the current [19].

Generally, heavy gases produce higher values of sputtering rate than light gases. Although Krypton is the best gas for sputtering, Argon is commonly used due to its low cost. Pressures involved are of the order of 1 torr [3].

Some applications require deposition rates higher than 1 \AA/s . This happens not only for economic reasons, but also for film structure reasons, since deposition rates influence the film microstructure and purity. This higher deposition rates can be achieved by the use of a magnetron discharge, which will be discussed later on the present chapter.

Sputtering pressure is a most important parameter in sputter deposition, in the sense that there is an ideal range of pressures that can be used in sputtering. Fig. 1.8 shows how the deposition rate varies with pressure in sputtering, and what the optimal operation conditions for the sputtering process are.

If the pressure is too low, the ions are produced far from the cathode (target) which vastly increases their chances of accumulating on the chamber walls. Also, the electron mean free path between collisions is considerably large and those electrons collected by the anode are not fully replaced by ion-impact secondary emissions on the cathode. Thus, at low sputtering pressures there is low ionisation efficiency, and it is not possible to maintain a self-sustained discharge for pressures under about 10 mTorr [18].

When maintaining the voltage, if one increases the sputtering pressure, what will happen is that the electron mean free path will decrease, more ions will be generated and a larger current will flow. This is when the best pressure conditions for sputtering are found.

In contrast, if the pressure inside the sputtering chamber is too high, the collisional scattering of the atoms will greatly increase, preventing them from depositing adequately.

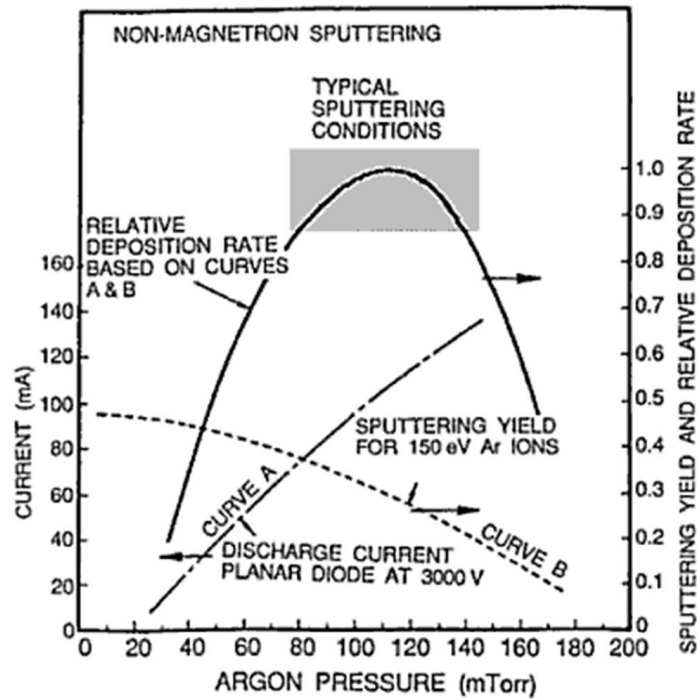


Fig. 1.8 Influence of working pressure and current on deposition rate for non-magnetron sputtering [18]

1.3. PLASMAS AND GASEOUS DISCHARGES

1.3.1. Plasmas

A plasma is a gas that is partially ionized which means that in a plasma there are three different types of particle populations: singly charged positive ions, electrons, and neutral gas particles. If most of the molecules or atoms in a certain region are ionised, the resulting state of matter is an overall electrically neutral gas, but which is microscopically composed of negatively charged electrons and positively charged ions. The plasma is

electrically conductive because negative and positive charges are able to move independently. This enables plasmas to respond strongly to electromagnetic fields. But also we must take into account that the density of charged particles in a plasma must be sufficiently large compared to the dimension of the plasma so that the coulombic interactions become significant [2]. Fig. 1.9 displays a perspective on the temperatures of plasmas, as well as their electron densities.

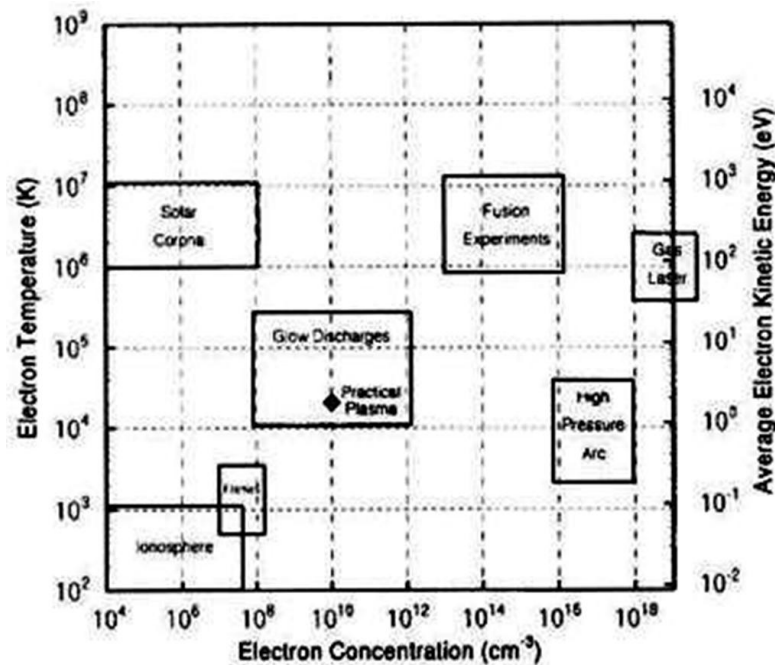


Fig 1.9 Plasma regimes: some approximate ranges of electron concentration and temperature for various types of plasma.[21]

The word “plasma” is a Greek word that means “to mould”. Irving Langmuir decided for this name in 1928 after observing that the positive column of his positive discharges conformed to the shape of their vessel. He then wrote: *"Except near the electrodes, where there are sheaths¹ containing very few electrons, the ionized gas contains ions and electrons in about equal numbers so that the resultant space charge is very small.*

¹A sheath is a volume space charge region (a region where the electrical charge density, ρ , is not equal to zero) that surrounds physical objects within the plasma and separates the plasma from the vacuum chamber walls.

We shall use the name plasma to describe this region containing balanced charges of ions and electrons." [20]

1.3.2. Glow Discharges for Sputtering

A discharge consists of a current flowing through a low-pressure gas. Plasmas are called glow discharges when there is a glow which results from light that is emitted from excited atoms. This is the case of the plasmas that are used in sputtering processes. Inside a sputtering chamber the target made of the material to be deposited is connected to the negative terminal (which is why it is also known as the cathode) of a power supply (DC or RF) and usually several kilovolts are applied to it. The substrate, which faces the target in the chamber, can be set in several ways: it may be grounded, biased negatively or positively, cooled, heated, or it might even present a combination of these.

Before the discharge takes place, the sputtering chamber is evacuated. Then a gas is introduced, typically argon, which will be the medium through which the discharge will take place. Gas pressure can range from a few to 100 mTorr, which is the necessary pressure to maintain the glow discharge regime (the most important regime in sputtering).

After a visible glow discharge, the gas is at an ionised state and the positive ions in the discharge collide with the target, transferring their momentum to neutral atoms of the target which are thus ejected before passing through the discharge region to eventually deposit on the substrate. But the neutral atoms are not the only species that are ejected from the target: the emission of secondary electrons, desorbed gases, negative ions and radiation (x-ray and photons) can also happen. Within these plasmas used in sputtering the ion and electron densities are essentially equal except in sheaths. Also particle density is low enough and fields are strong enough so that neutrals are not in equilibrium with electrons. The ratio between ions and neutrals is usually around 10^{-4} [2].

The electric field in the sputtering chamber will accelerate the negative ions and electrons toward the substrate, since they are forced to travel in the opposite direction of the target (which is connected to the negative terminal of the power supply). These negative ions will thus bombard the growing film.

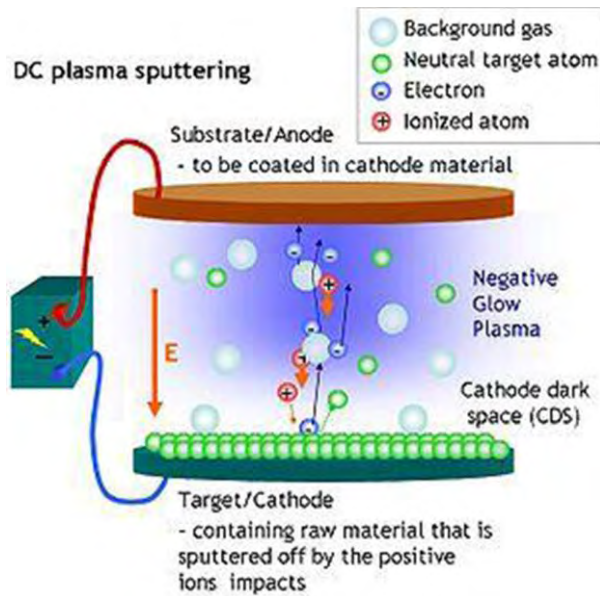


Fig. 1.10 Schematics of DC plasma sputtering

Fig. 1.10 shows a schematics of DC plasma sputtering. Energetic ions sputter material off the target which diffuses through the plasma towards the substrate where it is deposited. No strong plasma glows around cathode because it takes a certain distance for a few secondary electrons to create the plasma.

The environment of a glow discharge is not a simple one to model. The voltage is not the same at every point of the sputtering chamber, but it varies along the different areas between the electrodes (fig. 1.11). Inside the sputtering chamber there are different areas presenting different characteristics, some of them being extremely important in the optimization of the sputtering process. These will be described in more detail in the next section of the present chapter.

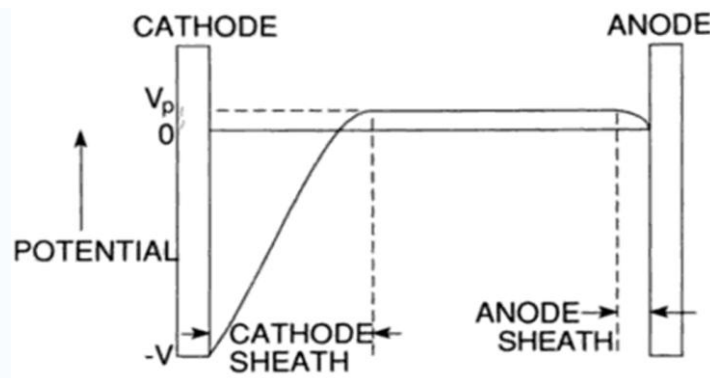


Fig. 1.11 Voltage distribution across DC glow discharge

1.4. SPUTTERING TECHNIQUES

This section aims to present and describe the basics of the fundamental sputtering processes. Particular attention will be given to the configuration of the equipment which performs this type of deposition.

It is important to mention that some modifications have been successfully introduced in the processes described below, such as the use of substrate bias to induce bombardment of the substrate and/or growing film, and thermionically assisted discharges [3].

1.4.1. DC Sputtering

There are several sputtering systems that can be used to produce thin films. The simplest sputtering process is the DC Sputtering, in which the system can be operated with DC current. This is considered a basic sputtering method since the other methods were created by introducing modifications to the DC Sputtering system in order to improve it [1].

The DC sputtering system is composed of two parallel planar electrodes. One of these electrodes is a cathode because it is connected to the negative terminal of a high-voltage DC power supply. Several kilovolts are usually applied to it [2]. The top plasma-facing surface of this electrode is covered with a target material and the reverse side is water-cooled. The sputtering target may have an area ranging from tens to several hundred square centimetres [3]. The other electrode, which faces the cathode, is called the anode. The anode receives the substrates. The walls of the vacuum chamber may also be a part of the anode. As already mentioned, the substrates may be grounded, electrically floating, biased positively or negatively, heated, cooled, or some combination of these [2]. Typically the electrodes are separated by few centimetres [3].

The DC sputtering happens in a DC glow discharge environment. In this discharge, before the application of the potential, gas molecules are electrically neutral and the gas at room temperature will contain very few if any charged particles. Occasionally however, a free electron may be released from a molecule by the interaction of, for example, a cosmic

ray or other natural radiation, a photon, or a random high energy collision with another particle.

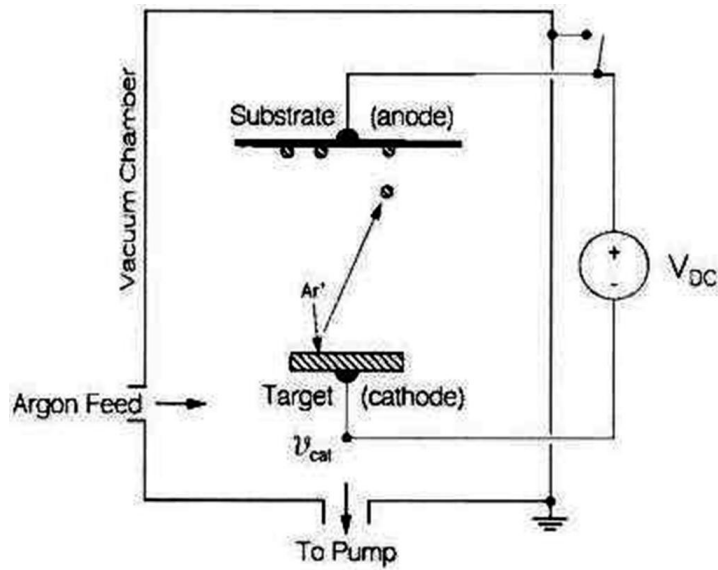
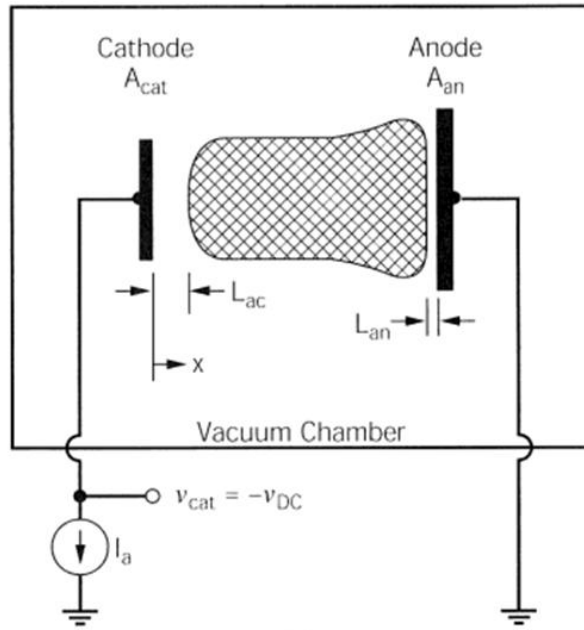


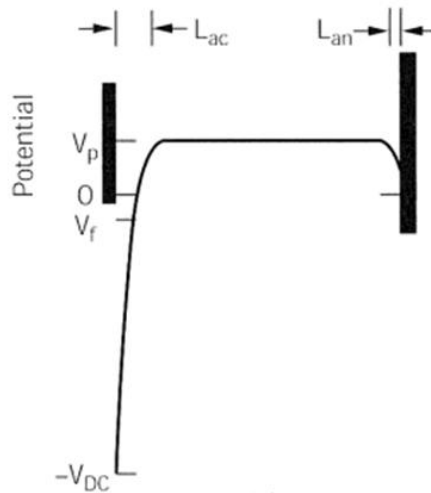
Fig. 1.12 Schematics of DC diode sputtering system [2]

A very small current flows at first due to the small number of initial charge carriers in the system. When a large voltage is applied between the electrodes, for instance in the order of 100 V/cm, any free electrons which may exist are quickly accelerated towards the anode. Thus, as the voltage increases, sufficient energy is imparted to the charged particles to create more carriers. This occurs through ion collisions with the cathode, which release secondary electrons, and by impact ionisation of neutral gas atoms. With charge multiplication, the current increases rapidly, but the voltage, limited by the output impedance of the power supply, remains constant. This regime is known as the Townsend discharge. Large numbers of electrons and ions are created through avalanches. Eventually, when enough of the electrons generated produce sufficient ions to regenerate the same number of initial electrons, the discharge becomes self-sustaining. The gas begins to glow, and the voltage drops (Fig. 1.13), accompanied by a sharp rise in current.

At this state “normal glow” occurs. Initially, ion bombardment increasingly spreads over the entire surface until a nearly uniform current density is achieved. A further increase in power results in higher voltage and current density levels. The “abnormal discharge” regime has now been entered, and this is the operative domain for sputtering. At still higher currents, low-voltage arcs propagate.



(a)



(b)

Fig. 1.13 a) Schematic diagram of a DC sputtering discharge;
 b) the potential profile (not to scale, as $V_p - V_f$ is typically much less than V_{DC})

A glow discharge progresses differently through distinct regions between the electrodes. The sequence of these discharge regimes is schematically displayed in Fig. 1.14.

Adjacent to the target (cathode) there is a highly luminous layer known as the cathode glow. The light emitted depends on the incident ions and the target material. In the cathode glow region, neutralisation of the incoming discharge ions and positive cathode ions occur. Secondary electrons start to accelerate away from the cathode in this area and collide with neutral gas atoms located some distance away from the cathode. In between is the Crookes dark space, a region where nearly all of the applied voltage is dropped. Within the dark space the positive gas ions are accelerated toward the cathode.

The next distinctive region is the “negative glow”, where the accelerated electrons acquire enough energy to impact-ionise the neutral gas molecules.

Beyond this is the Faraday dark space and finally the positive column. The substrate (anode) is placed inside the negative glow, well before the Faraday dark space so that the latter as well as the positive column do not normally appear during sputtering.

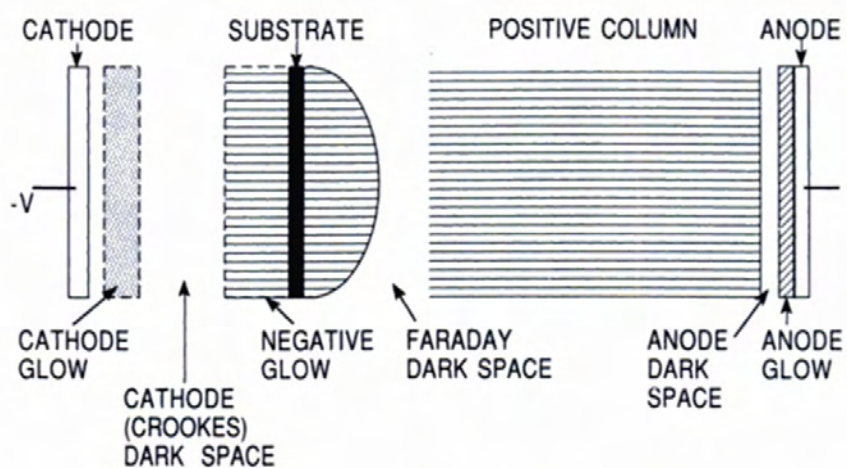


Fig. 1.14 Distinct regions of the DC glow discharge ^[2]

1.4.2. RF Magnetron Sputtering

1.4.2.1. RF Sputtering

Sputtering, as a deposition technique, encounters an important limitation in its DC mode: only conducting targets may be used in the process. Radio frequency sputtering, allowing the deposition of thin films using insulating targets, came as the solution for this constraint.

As a matter of fact, the surface of an insulator cannot be biased with a dc source given the non-conducting nature of the material. However, if one is able to make the surface of the insulator to be at a certain RF potential in relation to the plasma, this will result, then, in a *self*-bias by rectification [9]. Thus, RF sputtering works essentially due to the fact that the target *self*-biases to a negative potential, resulting from the fact that electrons are much more mobile than ions and are able to easily follow the periodic change in the electric field [2]. When the *self*-bias condition is observed, the target behaves like a dc electrode, with the plasma being created by the same atomistic processes as in DC sputtering.

Fig.1.15 shows a scheme of the essential arrangements of an RF sputtering system.

The power supply has usually a voltage up to 1 kV. Typical RF frequencies employed range from 5 to 30 MHz, and the most common value used is 13.56 MHz, which is the one established by the Federal Communications Commission for plasma processing [8].

Despite the fact that RF sputtering appeared as a solution for an important limitation of DC sputtering, the former is not entirely advantageous when compared with the later. RF sputtering presents lower deposition rates than DC sputtering [10]. However, this disadvantage can be neutralised by the combination of RF sputtering with Magnetron sputtering, which will be discussed in the following section.

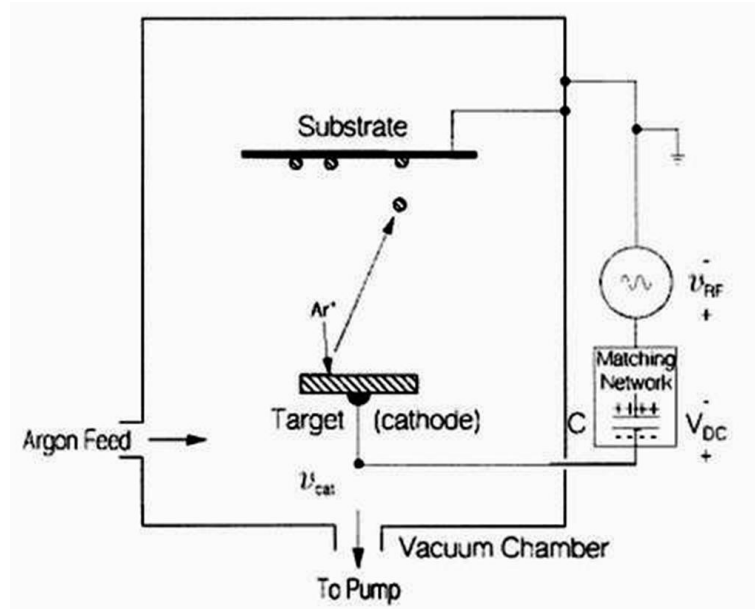


Fig.1.15 In RF sputtering there are typically a small area cathode (the target) and a larger area anode, in series with a blocking capacitor (C). The capacitor is actually part of an impedance-matching network that improves the power transfer from the RF source to the plasma discharge.

1.4.2.2. Magnetron Sputtering

Magnetron sputtering uses a magnetically assisted discharge. A permanent magnet is added to the sputtering arrangements in order to create a specially shaped magnetic field near the target. The magnetic field intensifies the plasma in that area by trapping electrons and enhancing ion bombardment of the target.

The trapping of electrons is achieved by $\mathbf{E} \times \mathbf{B}$ drift currents closing in on themselves [11]. The magnetic circuit behind the target forms a tunnel of semitoroidal magnetic field \mathbf{B} which, along with \mathbf{E} , creates a sort of endless racetracks where primary and secondary electrons are trapped, increasing greatly the chances of them colliding with a gas atom. Ion bombardment of the target becomes, thus, a much more efficient process and the impedance of the plasma drops, which will allow the use of much lower voltages: 500-600 V (or lower) compared to several kV [12]. Fig. 1.16 shows the effect of electron trapping on a target.

Several types of magnetron design can be used, namely planar magnetrons and S guns. Some of these designs are depicted in fig. 1.17. The first one is widely used due to its simplicity and ability to virtually extend the cathode (target) to any desirable size [12].

Planar magnetrons can, in their turn, present different magnet geometries (fig. 1.18).

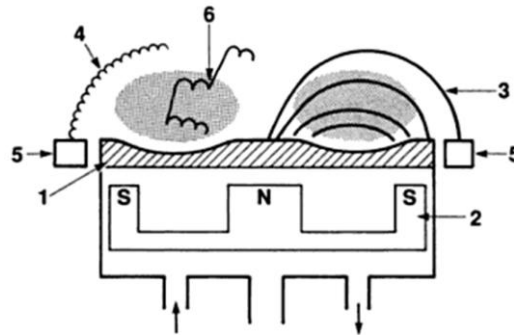


Fig. 1.16 Schematic of a target assembly with magnetron: (1) target showing erosion track under most intense plasma (2) magnets providing (3) magnetic field lines. Low energy electrons (4) reach the anode (5) along magnetic field lines while high energy electrons cross field lines by collision with gas atoms (6). [13]

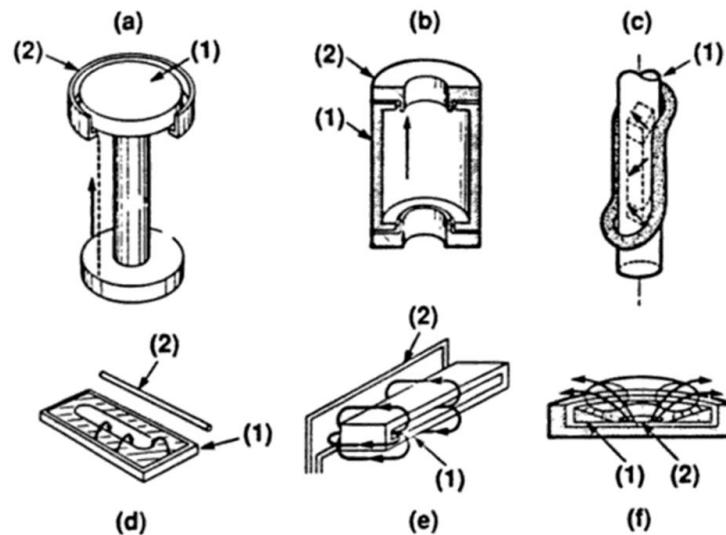


Fig. 1.17 Geometrical arrangements for magnetron sputtering: (a) cylindrical post (b) hollow cathode (c) lei (d) rectangular planar (e) belt (f) conical. The target (1) and the anode (2) are shown in each case; the electric field is normal to the target in each case. The heavy lines show the magnetic flux lines. [13]

Besides the already mention advantages that magnetron sputtering can bring, there is also the additional positive feature of allowing the use of lower sputtering gas pressure. However, it presents the disadvantage of more inhomogeneous target erosion [10].

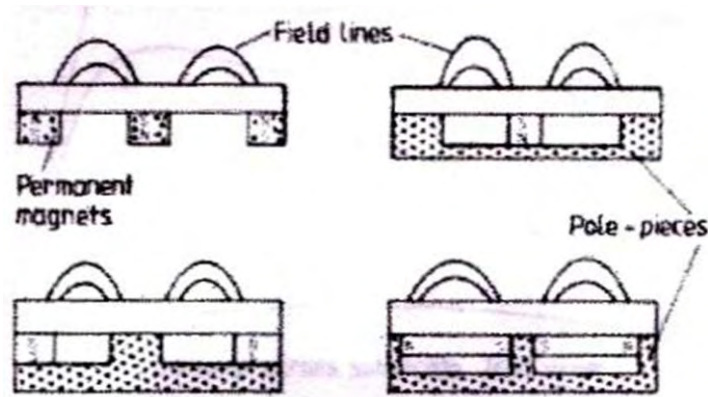


Fig. 1.18 Examples of possible magnet geometries in planar magnetrons [12]

1.5. SPUTTERING versus EVAPORATION

It is opportune to use this section to reflect on why sputtering was the deposition method chosen to produce the samples to be analysed. Facing the impossibility of including here an extensive comparison between sputtering and several others deposition methods, we chose to compare it with evaporation, which will hopefully provide a satisfactory explanation for our choice.

The most relevant characteristics of both methods are presented on table 1.1.

There we can see that, in several instances, sputter deposition presents significant advantages over evaporation. Sputtered particles have kinetic energies of 3-5 eV orders of magnitude above that of typical evaporated particles. This excess kinetic energy conveys a higher surface mobility to condensing particles, a relevant factor to obtain smooth and conformal film morphologies. Also, the typical relatively large area of the sputtering sources aids film thickness uniformity and conformality of coverage.

Another most relevant advantage of sputtering as a deposition technique is that, in most situations (mostly in metals and alloys) the deposited films have the same composition as the source material. Since the sputter yield depends on the atomic weight of the atoms in the target, one might expect faster sputtering of one of the components. However, since only surface atoms can be sputtered, the faster ejection of one element leaves the surface enriched with the others, efficiently cancelling out the difference in sputter rates. In contrast, evaporation may have different vapour pressures for each component, resulting in a deposited film with a different composition than the source.

Table 1.1 *Evaporation versus Sputtering* [2],[14]

	EVAPORATION	SPUTTERING
Mechanism	Thermal evaporation	Ion bombardment and collisional momentum transfer
Rate	Thousand atomic layers per second	Several atomic layers per second
Kinetic energy of atoms	Low	High
Choice of materials	Limited	Almost unlimited
Purity	Better (no gas inclusions, very high vacuum)	Possibility of incorporating impurities (due to the sputtering gas)
Substrate heating	Might be a problem for materials with high melting point	Unless magnetron is used, heating can be substantial
Target <i>in situ</i> cleaning	Not an option	Recommended
Alloy compositions, stoichiometry	Little or no control	Alloy composition can be tightly controlled
Changes in source material	Easy	Expensive
Decomposition of material	High	Low
Uniformity	Difficult	Easy over larger areas
Equipment	Low cost	More expensive
Number of depositions	Only one deposition per charge	Many depositions per target
Thickness control	Not easy to control	Very good, with several control possibilities
Adhesion	Often poor	Excellent
Film properties (e.g., grain size, step coverage)	Difficult to control	Control by bias, pressure or substrate heat

2. SHAPE MEMORY ALLOYS: Ni₂MnGa

Reversible structural deformations are an interesting feature in research for the development of new materials for engineering applications. Such deformations are characteristic of the shape-memory alloys (SMAs). While most current applications of these materials are related to a martensitic phase transformation driven by temperature, the magnetic control of such transformations would be faster and more efficient. [28] Heusler alloys, some of which are shape memory alloys, were mentioned for the first time in two published papers in 1903. They take the general compositional formulae X₂MnY, where X and Y represent elements from the d and p blocks of the periodic table. In most cases, these alloys crystallise in well ordered structures based upon the fcc lattice [29]. Ni₂MnGa is an example of a SMA which exhibits ferromagnetic behaviour. This magnetic behaviour can be controlled by temperature, moderate magnetic fields, stress and combinations of the previous [38]. Ni₂MnGa and other materials with the same characteristics are generally called ferromagnetic shape memory alloys (FSMAs). For Ni₂MnGa the martensitic transformation temperature (T_m) is around 200 K, and the ferromagnetic behaviour occurs below the Curie temperature (T_C) which is around 370 K.

In recent years, Ni₂MnGa FMAs have attracted great attention due to their applicability to micro-electromechanical systems (MEMS). Because they present fast response frequency and giant reversible magnetic-field-induced strain (MFIS) of around 7% [44], they are thought of as a new kind of material for these devices, as long as they are able to comply with the need of miniaturisation that they require. This need has led the development of the study to Ni₂MnGa thin films.

The martensitic transformation is a diffusionless transformation where the change in crystal structure is achieved by a deformation of the parent phase [31]. This transformation has been well documented in bulk Ni₂MnGa, as well as the effect of composition on the temperature at which this transformation occurs. Studies performed for films with a composition of Ni_{2+x}MnGa_{1-x} related that the martensitic transformation temperature (T_m) increases linearly with increasing x [33]: for x=0 (stoichiometric composition, Ni₂MnGa), T_m is approximately 200K, whereas for x = 0.18-0.19, T_m shows values between 320K and 330K.

Composition does not only influence strongly the martensitic phase temperature, but also its crystalline structure or specific structural modulation, as well as the magnetic

behaviour of the alloy. For instance, for a composition of $\text{Ni}_{2+x}\text{Mn}_{1-x}\text{Ga}$ (excess of Ni over Mn) three different regions can be distinguished on the plot of T_m and T_c versus x (fig 2.1) [43]. When $x \leq 0.16$, $T_c > T_m$ and the martensitic transformation takes place when in the ferromagnetic state. Alloys for which $0.18 \leq x \leq 0.27$ are characterized by a coupled magnetostructural transition, i.e., $T_m \approx T_c$. Finally, the third region, where $x \geq 0.30$, is characterized by a high martensitic transformation temperature, $T_m \approx 550$ K. In this region the martensitic transformation takes place when in the paramagnetic state. The occurrence of the high temperature martensitic transformation makes alloys from this region attractive for application as high temperature shape memory alloys.

A study of the phases involved in Ni_2MnGa martensitic transformation was first reported in 1984 by Webster et al. [30]. From that study came the conclusions stating that in this thermo-elastic transformation, which is present when cooling the material below 220K, the parent cubic phase stable at high temperature belongs to Fm-3m space group, with a $L2_1$ structure which lattice parameter is $a_a = 5.833 \text{ \AA}$.

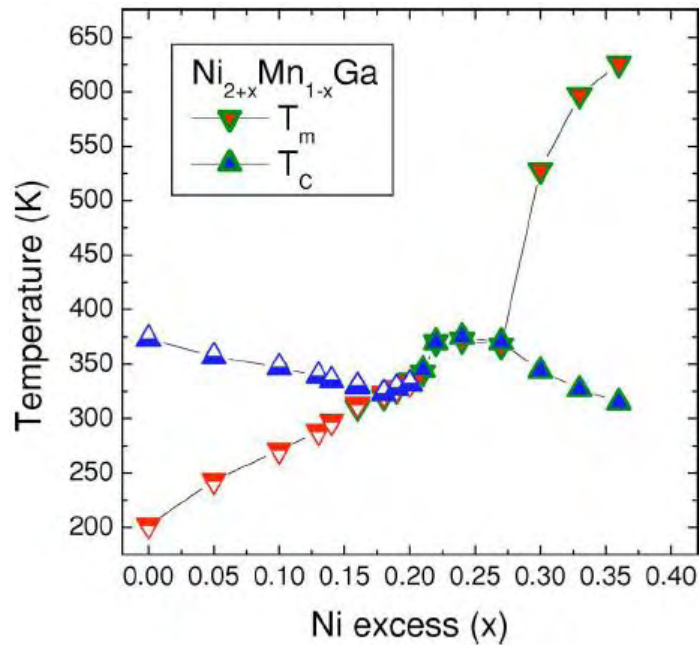


Fig. 2.1 Experimental phase diagram of $\text{Ni}_{2+x}\text{Mn}_{1-x}\text{Ga}$ $0 \leq x \leq 0.36$ constructed from DSC and magnetization measurements [43]

This homogeneous deformation starts as a mechanism described by Bain in 1924, generally called “Bain strain” and it is depicted on Fig. 2.2 [31]. It consists of a contraction

of the c -axis accompanied by the elongation of the other two vectors. The cell parameters of Ni₂MnGa martensitic structure (referred to the austenite L2₁) lattice are $a_m=5.920\text{\AA}$ and $c_m=5.566\text{\AA}$ [32]. But the Bain strain mechanism is not enough to fully describe the martensitic transformation, there is additionally a rotation through an angle θ (Fig. 2.3).

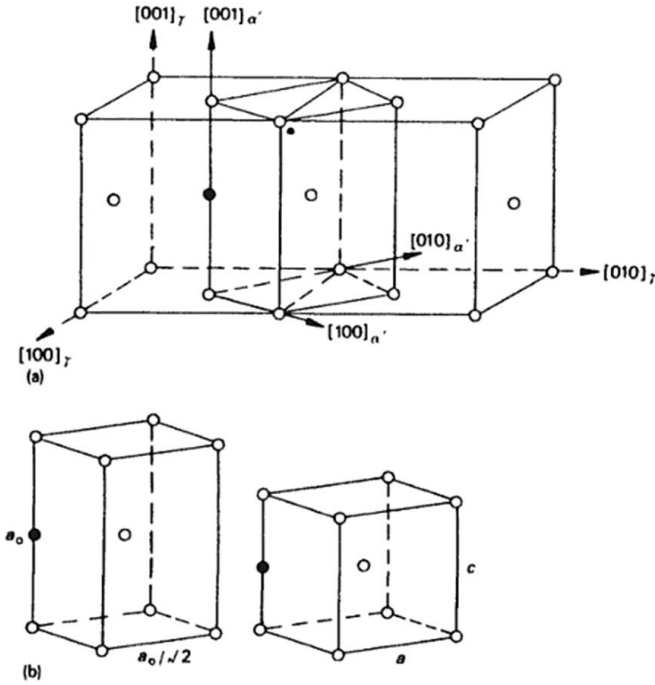


Fig. 2.2 The lattice correspondence for the formation of martensite from austenite: (a) tetragonal unit cell outlined in austenite, (b) lattice deformation [31]

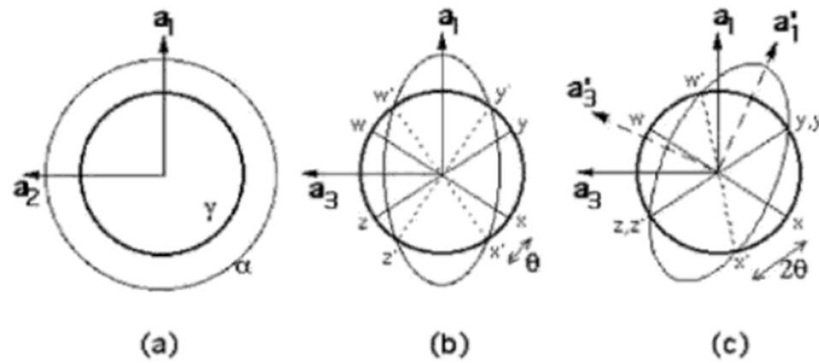


Fig. 2.3 (a) and (b) show the effect of the Bain strain on austenite and (c) shows the rotation through an angle θ . a_1 , a_2 and a_3 refer to $[100]_\gamma$, $[010]_\gamma$ and $[001]_\gamma$ axes, respectively. [34]

The symmetry of the structure of the product of such a transformation can be described as a body-centred unit cell obtained from the parent fcc lattice by applying the following transformation:

$$\begin{pmatrix} \mathbf{a}_m \\ \mathbf{a}_m \\ \mathbf{c}_m \end{pmatrix} = \begin{pmatrix} 1/2 & -1/2 & 0 \\ 1/2 & 1/2 & 0 \\ 0 & 0 & 1 \end{pmatrix} \begin{pmatrix} \mathbf{a}_a \\ \mathbf{a}_a \\ \mathbf{c}_a \end{pmatrix}. \quad (2.1)$$

In Fig. 2.2 we can see that the tetragonal lattice has the fundamentals parameters coinciding with the [1-10], [110] and [001] directions of the L21 superstructure. For the Ni_2MnGa material the lattice parameters become $a_m = 4.186\text{\AA}$ and $c_m = 5.566\text{\AA}$ [32].

The application of a magnetic field to these materials does not only influence the martensitic transformation temperature, but it can also induce a reorientation of martensite variants in twinned martensites with high magneto-crystalline anisotropy energy, as shown in fig. 2.4. This phenomenon is what we already referred to as the magnetic shape memory effect.

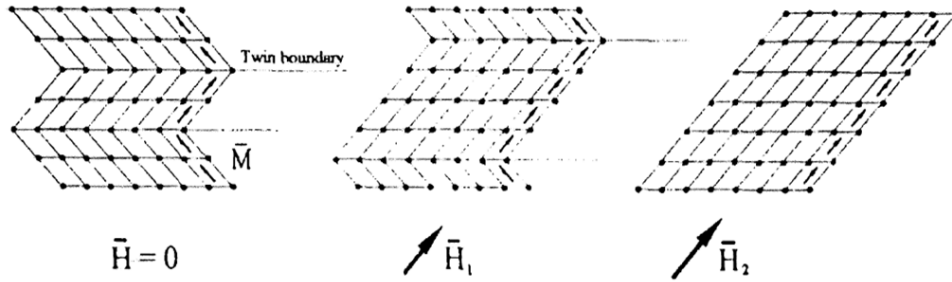


Fig. 2.4 Schematic illustration of the magnetic shape memory effect ($H_2 > H_1$) [37]

The magnetic properties of the Ni_2MnGa system in thin films are not yet fully understood. It is known that temperature and magnetic field dependences of magnetisation show hysteresis caused by strong magnetic and structural coupling of subsystems [33]. It is also known that the magnetic properties vary, to a certain extent, as a function of the film thickness [34] and that the Curie temperature for this material depends on the film composition. Studies performed for films with a composition of $\text{Ni}_{2+x}\text{MnGa}_{1-x}$ related that

the Curie temperature (T_C) decreases almost linearly with increasing x [33]: for $x = 0$ (stoichiometric composition, Ni_2MnGa), T_C is approximately 370K, whereas for $x = 0.18$ - 0.19 , T_C matches the value of T_m .

The change of magnetic moment during the martensitic transformation is an important factor, since it determines the martensitic transition temperature for a certain value of the applied field, which is a fundamental feature in many MSMAs applications. It is established that the magnetisation decreases smoothly with an increasing temperature, and that it shows an abrupt change when the temperature reaches a critical value. This critical value has been reported [30][35][36] to be the temperature for which the material undergoes the structural phase transformation from martensite to austenite, or, T_m , as we have previously named it. However, some aspects of the change of magnetic moment during the martensitic transformation are not yet clear, which is one of the reasons why it is important to persist on the investigation of the magnetic properties of the MSMAs.

It is opportune to comment, as a final note, that the Ni_2MnGa alloys also possess other technologically interesting properties regarding giant magneto-caloric and giant magneto-resistance (abrupt change in the resistance of the material as a response to an applied magnetic field [41]) properties. The magnetocaloric effect in these materials is essentially related to magnetic induced phase transitions. There is therefore a considerable change of entropy controlled by a magnetic field, which opens the way to applications [40].

3. EXPERIMENTAL DETAILS

3.1. SAMPLE FABRICATION

The Ni-Mn-Ga thin films were sputtered with a radio frequency (RF) magnetron sputtering device on well-cleaned substrates of glass, Al₂O₃ (0001), Si (100), SrTiO₃ (100) and MgO (100).

The sputtering system consists of two magnetrons cooled with water, each attached to a circular target, a RF source, a heating source to set the temperature of the substrates, which were fixed on a substrate holder. Also a part of this sputtering system is the vacuum equipment which allowed the control of the atmosphere inside of the deposition chamber. The cleaning of the substrates involved two steps. The first one consisted of 10 minutes in an ultrasonic bath of acetone to remove any existing grease. Water was not used because it is absorbed, for instance, by the MgO substrate. The second step consisted in removing the acetone from the substrates by immersing them in an ultrasonic bath of ethanol for 10 minutes.

The deposition was performed using two circular targets, Ni₅₀Ga₅₀ and Ni₅₀Mn₅₀, with a 2 inch diameter each. The Ni₅₀Mn₅₀ target is from Testbourne Ltd and the Ni₅₀Ga₅₀ target is from ACI Alloys, Inc.

The initial existing pressure in the sputtering chamber (before argon was released) was always below 1×10^{-7} mbar. In the work presented the films were deposited under different argon (Ar) pressures, namely, 2.5×10^{-3} , 5.0×10^{-3} and 7.0×10^{-3} mbar, and using different sputtering powers for each target. Other sputtering parameters varied in the deposition of the Ni-Mn-Ga samples were sputtering time and substrate temperature. Table 3.1 summarises the characteristics of the substrates used for each sample and their temperature during the deposition process. Table 3.2 lists the sputtering conditions for each sample.

Table 3.1 *Substrate characteristics for each produced sample*

SAMPLE	SUBSTRATE				
	Type	Surface Cut	Dimensions (mm ³)	T _{deposition} (°C)	Lattice Parameter (Å)
NMG6g	Glass	-	30x30x1	450	-
NMG8g	Glass	-	30x30x1	450	-
GMN9a	Al ₂ O ₃	0 0 0 1	10x10x0,5	540	4.759
GMN9b	Si	1 0 0	10x10x0,5	540	5.431
GMN9c	SrTiO ₃	1 0 0	10x5x0,5	540	3.905
GMN9d	MgO	1 0 0	10x5x0,5	540	4.215
NMG11a	Al ₂ O ₃	0 0 0 1	10x10x0,5	420	4.759
NMG11b	Si	1 0 0	10x10x0,5	420	5.431
NMG11c	SrTiO ₃	1 0 0	10x5x0,5	420	3.905
NMG11d	MgO	1 0 0	10x5x0,5	420	4.215
NMG12a	Al ₂ O ₃	0 0 0 1	10x10x0,5	400	4.759
NMG12b	Si	1 0 0	10x10x0,5	400	5.431
NMG12c	SrTiO ₃	1 0 0	10x5x0,5	400	3.905
NMG12d	MgO	1 0 0	10x5x0,5	400	4.215
NMG13a	Al ₂ O ₃	0 0 0 1	10x10x0,5	420	4.759
NMG13b	MgO	1 0 0	10x5x0,5	420	4.215
NMG13c	SrTiO ₃	1 0 0	10x5x0,5	420	3.905
NMG13d	Si	1 0 0	10x10x0,5	420	5.431

Table 3.2 Sputtering deposition parameters for each produced sample

SAMPLE	SPUTTERING				Time (min)
	Ni ₅₀ Ga ₅₀		Ni ₅₀ Mn ₅₀		
	Power (W)	Power Density (W/cm ²)	Power (W)	Power Density (W/cm ²)	
NMG6g	11	0,54	16	0,79	90
NMG8g	10	0,49	13	0,64	120
NMG9a	8	0,39	10	0,49	102
NMG9b	8	0,39	10	0,49	102
NMG9c	8	0,39	10	0,49	102
NMG9d	8	0,39	10	0,49	102
NMG11a	14	0,69	16	0,79	90
NMG11b	14	0,69	16	0,79	90
NMG11c	14	0,69	16	0,79	90
NMG11d	14	0,69	16	0,79	90
NMG12a	14	0,69	16	0,79	90
NMG12b	14	0,69	16	0,79	90
NMG12c	14	0,69	16	0,79	90
NMG12d	14	0,69	16	0,79	90
NMG13a	14	0,69	14	0,69	17
NMG13b	14	0,69	14	0,69	17
NMG13c	14	0,69	14	0,69	17
NMG13d	14	0,69	14	0,69	17

3.2. CHARACTERISATION

3.2.1. Energy dispersive x-ray spectroscopy (EDS)

The stoichiometry of the samples was measured with the collaboration of Prof. Pedro Tavares at the University of Trás-os-Montes e Alto Douro (UTAD), with the EDS/SEM (scanning electron microscope) Philips-FEI/Quanta 400 system. These measurements were made after preparation of the samples, which were attached with carbon tape to aluminium pins. The conditions at which the measurements were performed were: high vacuum mode, partial pressure inside the chamber of 1.33 mbar and an acceleration tension of 30 kV. These measurements possess an accuracy of 0.1%.

3.2.2. SEM

SEM images can provide important information on the morphology of materials. In the case of materials deposited as thin films, not only it is possible to obtain information on the surface roughness, for instance, but it is also possible to evaluate the homogeneity of these films. Several SEM images of the Ni₂MnGa thin films were collected with the EDS/SEM Philips-FEI/Quanta 400 system referred on the previous section.

3.2.3. X-ray diffraction (XRD) and X-ray reflectivity (XRR) measurements

X-ray diffraction results from the scattering or bending of X-rays as they pass obstacles and interference. This technique provides us with a lot of information on the structure of crystalline solids. Atoms in a crystal form a periodic array of obstacles that scatter x-rays coherently. The reason to use this type of radiation is that an x-ray's wavelengths are similar to the distance between atoms of the crystal. Diffraction from different planes of atoms produces a diffraction pattern, which will provide information about the structure of the crystal. The XRD spectra taken for thin films contain peaks which belong to their substrates. It is thus necessary to analyse the substrate XRD spectrum in order to identify its peaks on the thin film XRD spectrum and separate them.

X-ray reflectivity is a technique used for the calculation of density, thickness and roughness of thin film structures (whether they are single or multi-layered). It is based on total external reflection of X-rays from surfaces and interfaces. This technique will only be effective as long as there is a contrast between the electron densities of different layers and it is very sensitive to surface characteristics.

XRD and XRR measurements were performed with $\text{CuK}\alpha$ radiation in an X'Pert PRO MRD system from PANALYTICAL. The measurements were carried out with the x-ray source set at a voltage of 40 kV and a current of 50 mA .

3.2.4. Vibrating Sample Magnetometer (VSM)

A VSM is an instrument used to measure magnetic properties of samples, such as magnetisation. This instrument performs measurements of the sample magnetisation as a function of the magnetic field strength and temperature. The sample placed inside a VSM device is vibrated in a uniform magnetising field. The vibration of the magnetised sample induces an electrical signal in stationary pick-up coils placed conveniently, which is proportional to the magnetic moment, the vibrational amplitude and the vibrational frequency of the sample [39]. The measurements of magnetisation as a function of the applied magnetic field were performed in a VSM equipment of CRYOGENIC Limited, with a resolution of 5×10^{-5} emu. The measurement ranges are 1.5 to 320 K and -10 to +10 T , for temperature and magnetic field, respectively. The films were all positioned in plane to the field.

The measurements of the magnetisation of the studied Ni_2MnGa samples contain a magnetisation contribution from the substrate which is diamagnetic. This means that this contribution will have to be subtracted from the results obtained directly from the VSM equipment. This process will be explained in more detail in the section “Results and discussion”.

4. RESULTS AND DISCUSSION

This chapter contains the results of the measurements performed in order to characterize the structure and analyse the magnetic behaviour of the Ni₂MnGa thin films, and ultimately to establish a relation between the two. The first section of the present chapter is dedicated to the compositional analysis of the aforementioned films, followed by a second section containing their SEM pictures. The third section contains the results of x-ray measurements, which are divided in two separate groups: the x-ray reflectivity measurements and the x-ray diffraction measurements (XRD). A fourth section contains the results of VSM measurements, as well as their description and interpretation. The last section of this chapter shows the results of ferromagnetic resonance measurements for samples #12a and #12b.

The thicknesses of the films were estimated by X-ray reflectivity measurements, and their composition was studied using the aforementioned EDS/SEM system. X-ray diffraction measurements were performed to investigate the crystal structure of the films.

4.1. EDS

In this section we present the results of the composition of most of the thin films studied, which was obtained with the aforementioned EDS/SEM system and conditions.

Several samples were sputtered under the same sputtering conditions: same sputtering power and Ar pressure. Table 4.1 enables us to make a few considerations on the composition of the samples and their sputtering parameters.

Samples #6g and #7g were sputtered on the same substrate and under the same sputtering conditions, except for a small increase in the power of the NiGa substrate for sample #6g. It is noticeable, as expected, that such increase translates in a considerable increase in the percentage of Ga and a decrease in the percentage of Mn.

In the case of #9a and #9b, a change of substrate from Al₂O₃ to Si introduces a decrease and an increase in the percentages of Ni and Mn, respectively, whereas the percentage of Ga remains unchanged. However, in the case of the same change in substrate, but this time for samples #12a and #12b (different sputtering conditions from #9a and #9b), the percentage decreases for Mn and increases for Ga.

Table 4.1 Composition of the samples and corresponding sputtering parameters

SAMPLES	COMPOSITION (%)			Ar pressure ($\times 10^{-3}$ mbar)	Sputtering power (W)
	Ni	Mn	Ga		
NMG6g	55,4	28,0	16,6	5	11
NMG8g	54,0	24,4	21,6	5	12
NMG9a	53,5	19,7	26,8	7	8
NMG9b	53,3	19,9	26,8	7	8
NMG11a	56,5	18,9	24,6	5	14
NMG11b	55,4	19,6	25,0	5	14
NMG11c	55,8	18,7	25,5	5	14
NMG11d	55,3	19,7	25,0	5	14
NMG12a	56,2	18,9	24,9	2.5	14
NMG12b	55,7	18,6	25,7	2.5	14
NMG12c	57,0	18,0	25,0	2.5	14
NMG12d	57,1	21,2	21,7	2.5	14
NMG13a	54,8	19,0	26,2	5	14
NMG13b	57,8	20,9	21,3	5	14
NMG13c	56,2	25,2	18,6	5	14

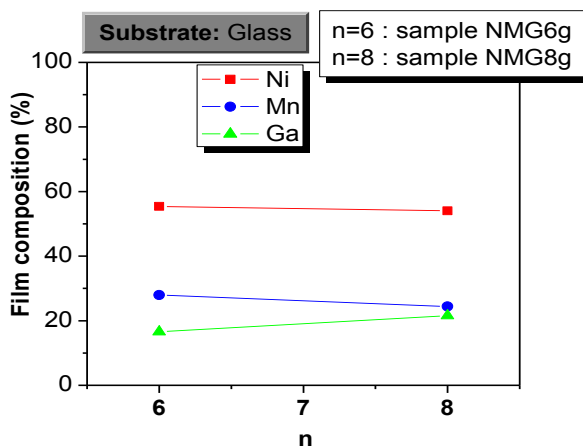


Fig. 4.1 Composition of samples NMG6g and NMG8g

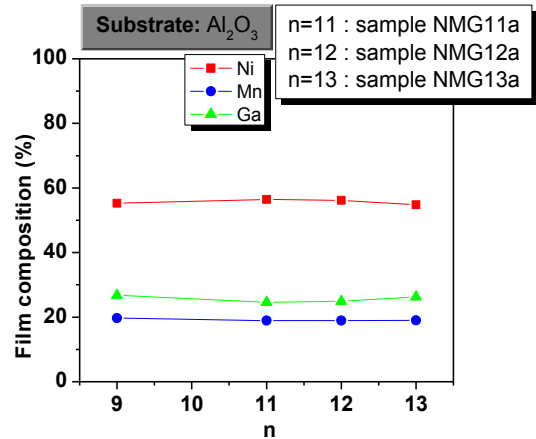


Fig. 4.2 Composition of samples NMG11a, NMG12a and NMG13a

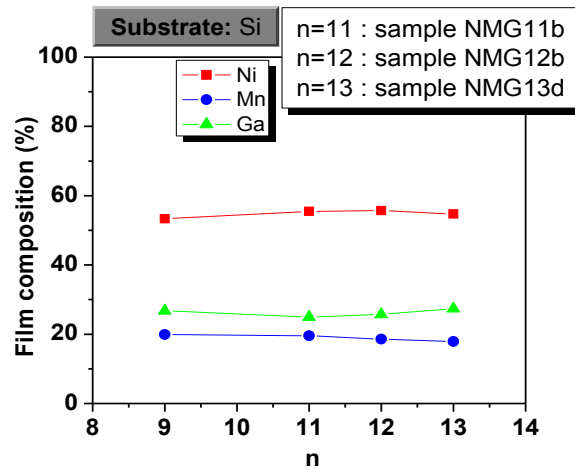


Fig. 4.3 Composition of samples NMG11b, NMG12b and NMG13d

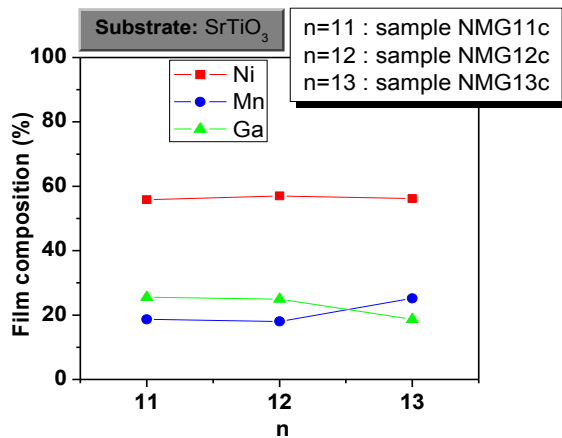


Fig. 4.4 Composition of samples NMG11c, NMG12c and NMG13c

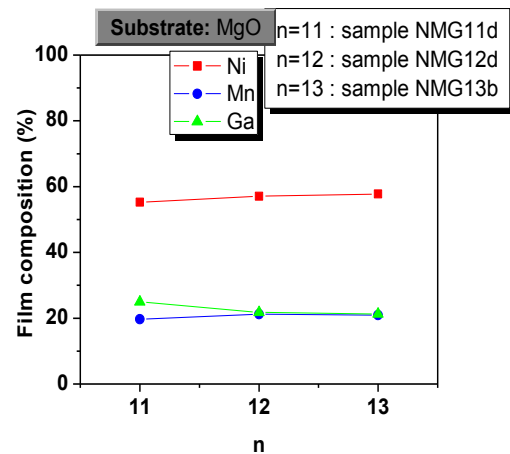


Fig. 4.5 Composition of samples NMG11d, NMG12d and NMG13b

4.2. SEM

This section contains the SEM images of the Ni₂MnGa thin films under study. They provide information on the characteristics of the film's surface, like its roughness and homogeneity.

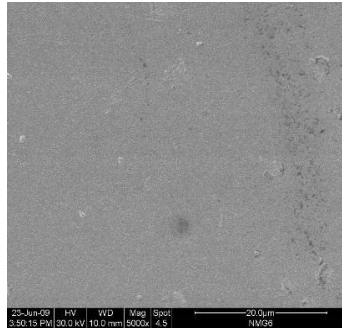


Fig. 4.6 Sample NMG6g, magnification 5000x

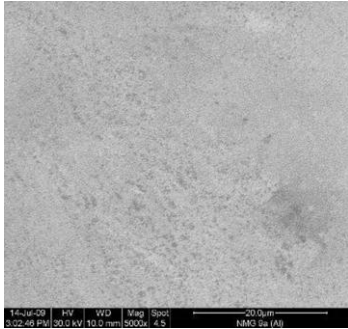


Fig.4.7 Sample NMG9a, magnification 5000x

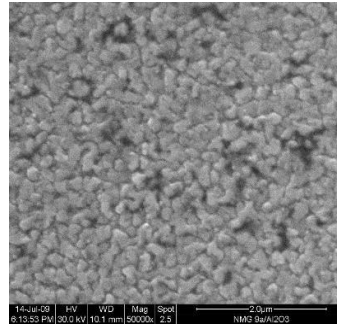


Fig.4.8 Sample NMG9a, magnification 50000x

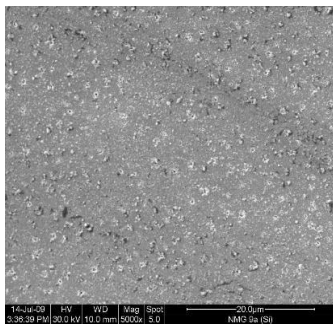


Fig.4.9 Sample NMG9b, magnification 5000x

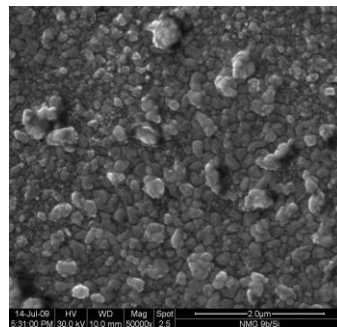


Fig.4.10 Sample NMG9b, magnification 50000x

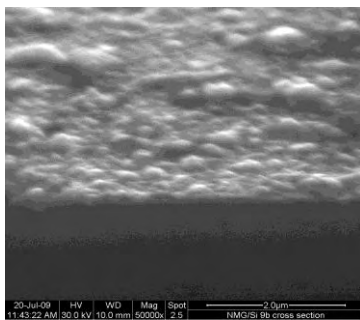


Fig.4.11 Sample NMG9b, cross section, magnification 50000x

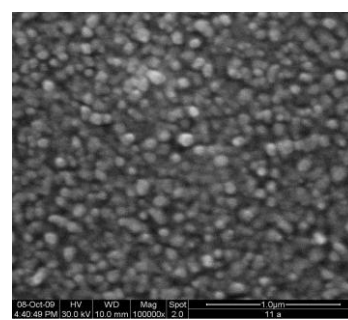


Fig.4.12 Sample NMG11a, magnification 100000x

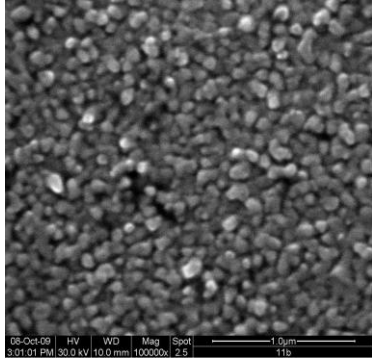


Fig.4.13 Sample NMG11b, magnification 100000x

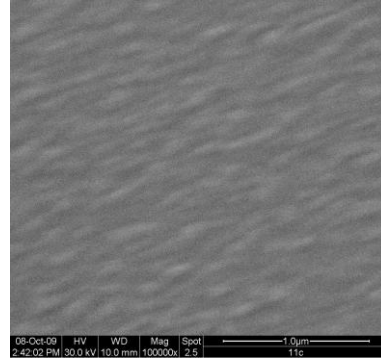


Fig.4.14 Sample NMG11c, magnification 100000x

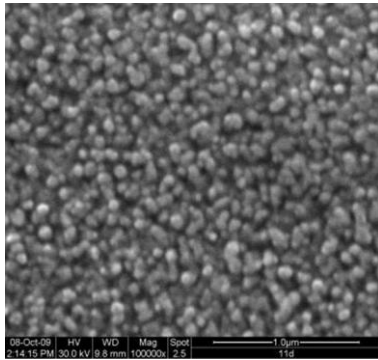


Fig.4.15 Sample NMG11d, magnification 100000x

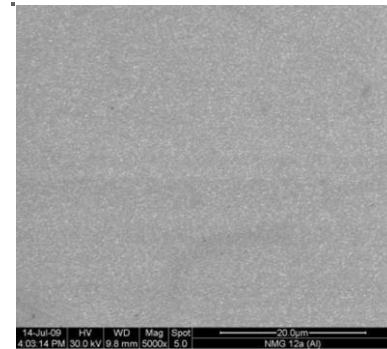


Fig.4.16 Sample NMG12a, magnification 5000x

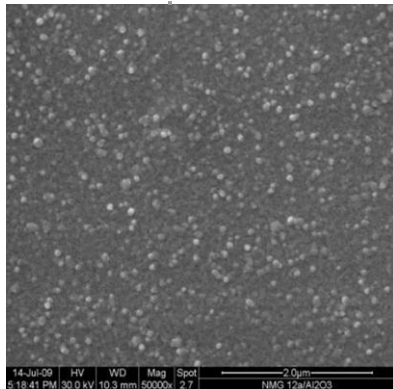


Fig.4.17 Sample NMG12a, magnification 50000x

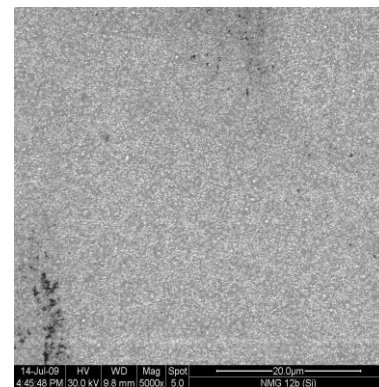


Fig.4.18 Sample NMG12b, magnification 5000x

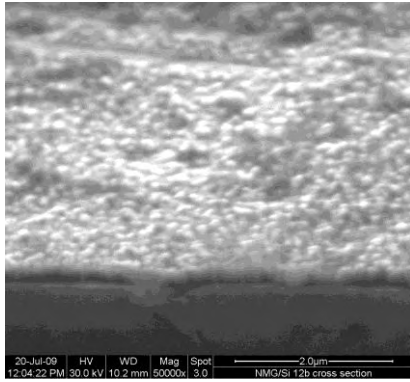


Fig.4.18a Sample NMG12b, cross section, magnification 50000x

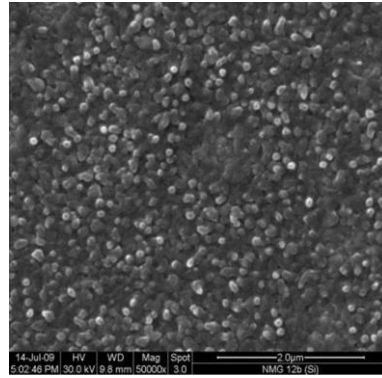


Fig.4.19 Sample NMG12b, magnification 50000x

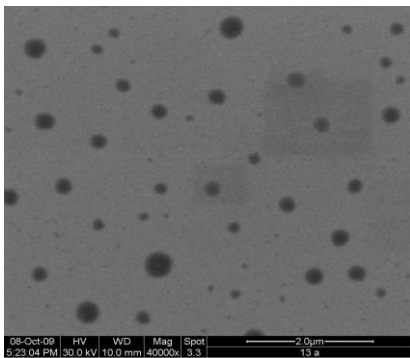


Fig.4.20 Sample NMG13a, magnification 40000x

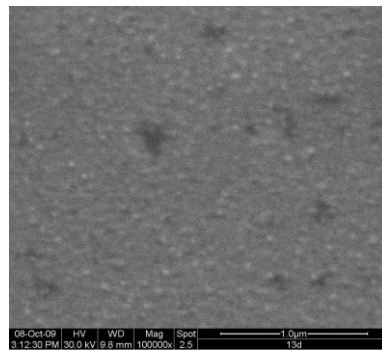


Fig.4.21 Sample NMG13d, magnification 100000x

These SEM pictures give us an idea of the characteristics of the film's surface. The spots on fig. 4.20 are a result of solvent condensation used in a deficient cleaning of the film. We can distinguish grains in most samples, ranging from an average size of 0.08 to 0.36 μm , for samples #11d and #9b, respectively. An estimation of the size of the grains observed in these images can give us an idea of the roughness and homogeneity of the films' surfaces. We can thus expect higher surface roughness for the #9b sample for being the sample to show bigger grains on the surface. On the other hand, sample #13d shows no measurable grains on a SEM image with a magnification of 100000x, which means that this sample possesses the smoothest surface of all samples. These estimations are confirmed by the x-ray reflectivity measurements which are shown on the next section of the present chapter.

4.3. X-RAY MEASUREMENTS

This chapter will first outline the results from x-ray reflectivity measurements performed to obtain insightful information on three different aspects which characterise the thin films under study: thickness, density and roughness. A second section will present the results from XRD measurements which are useful to characterise the structure of the films, for they allow the calculation of the phase(s) present on the sample and the respective lattice parameters. In both cases, the measurements were made using a voltage of 40 kV and an electric current of 50 mA. The wavelength of the x-rays used was 1.5406 Å.

4.3.1 X-ray reflectivity measurements (XRR)

Fig. 4.23 shows the x-ray reflectivity measurements performed on samples #9a, #9b, #13a, #13b, #13c and #13d.

The thickness of a thin layer can be determined from the angle positions of the consecutive maxima of the reflectivity curve. These maxima, called the *Kiessig fringes*, are caused by the interference of waves which are reflected at the top and bottom interfaces of the layer. Using the reflectivity formula for a layer deposited onto a semi-infinite substrate and Snell's law, we are able to obtain the following expression:

$$\alpha_m^2 = \alpha_c^2 + \left(\frac{m \lambda}{2d}\right)^2 \quad (4.1)$$

where α_m is the angle corresponding to the m^{th} reflectivity maximum, α_c is the critical angle, λ is the wavelength of the x-ray used in the reflectivity measurements and d is the thickness of the layer. Performing a plot of α_m as a function of m^2 , we can obtain the film thickness from its slope. Fig. 4.23 shows an example of such a plot for sample #13b. With the obtained slope value of approximately $5,1 \times 10^{-6}$ after performing a linear fitting to the plot, it is easy to obtain the approximate value of 35 nm for the #13b film thickness, d . With the obtained slope value of approximately $5,1 \times 10^{-6}$ after performing a linear fitting to the plot, it is easy to calculate the film thickness, d , which is of 35 nm for the #13b film.

Table 4.2 shows the results of these calculations for samples #9a and #9b, and #13a to #13d. These values thus calculated are average values for each series of samples and should be understood as a rough approximation of the thicknesses of the films.

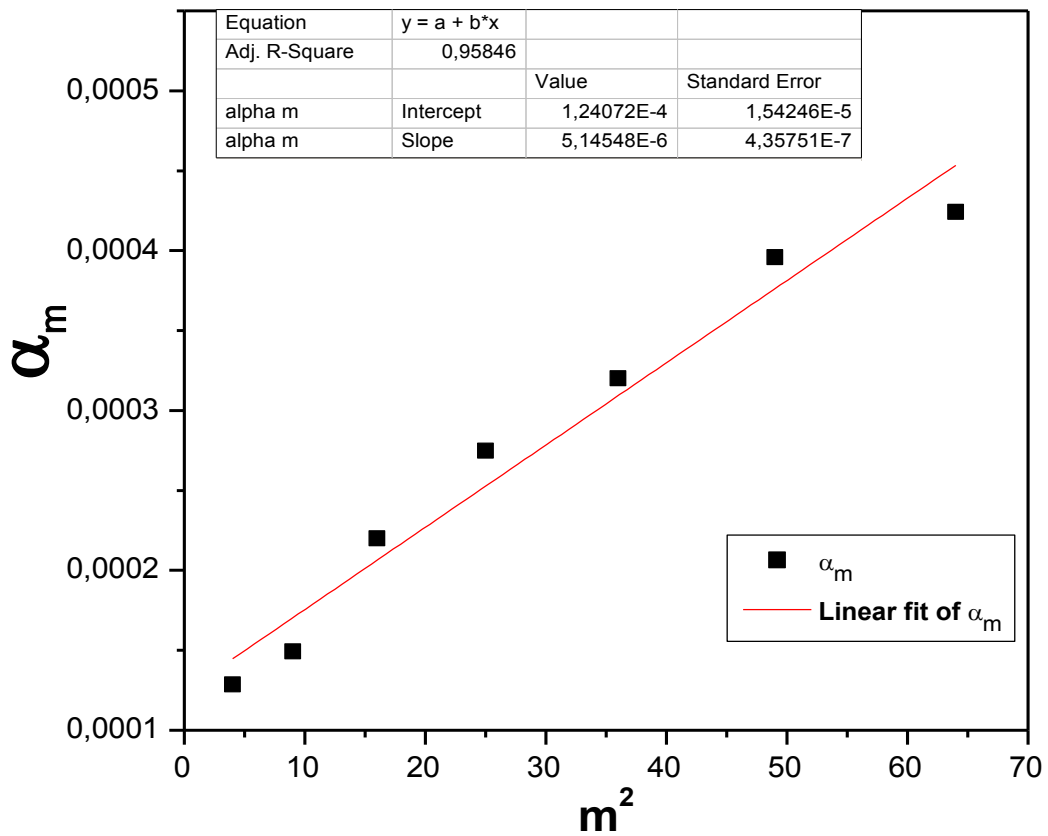


Fig.4.22 Plot of α_m vs m^2 for sample NMG13b

Table 4.2 Thicknesses of the samples for which XRR measurements were performed

SAMPLES	THICKNESS (nm)
NMG9a	80 ± 5
NMG9b	80 ± 5
NMG13a	35 ± 5
NMG13b	35 ± 5
NMG13c	35 ± 5
NMG13d	35 ± 5

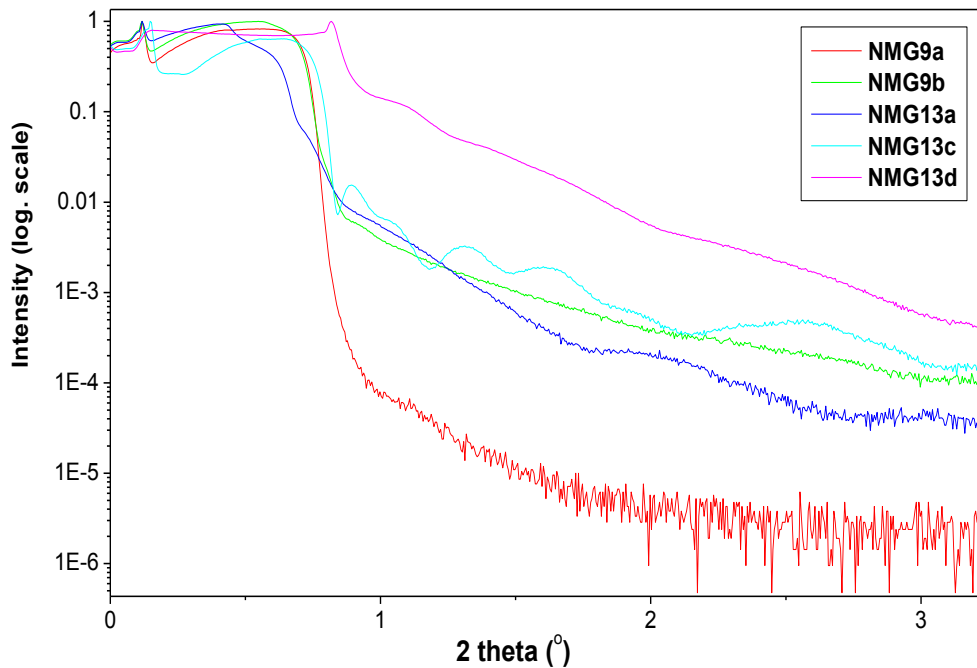


Fig. 4.23 X-ray reflectivity measurements performed on samples NMG9a, NMG9b, NMG13a, NMG13b, NMG13c and NMG13d

X-ray reflectivity (XRR) measurements also allow us to conclude about the roughness of the films' surfaces. It is known that the dampening of the Kiessig fringes is caused by the roughness of the reflecting interface. The higher the degree of roughness of the surface, the more abruptly drops the intensity of the reflected ray. In fig. 4.23 we can observe the decrease on the same plot in intensity for every measured sample and thus it is possible to conclude that samples #9a and #13d possess the roughest and the smoothest surface, respectively. If considered relevant, it is possible to estimate quantitatively the roughness of the surface using appropriate models, but the special software available to perform that kind of calculation was not used in this preliminary study.

4.3.2 XRD measurements

Figs. 4.25-28 show the XRD spectra for several of the samples aggregated according to their substrate with a logarithmic vertical scale (not shown for simplicity of plots).

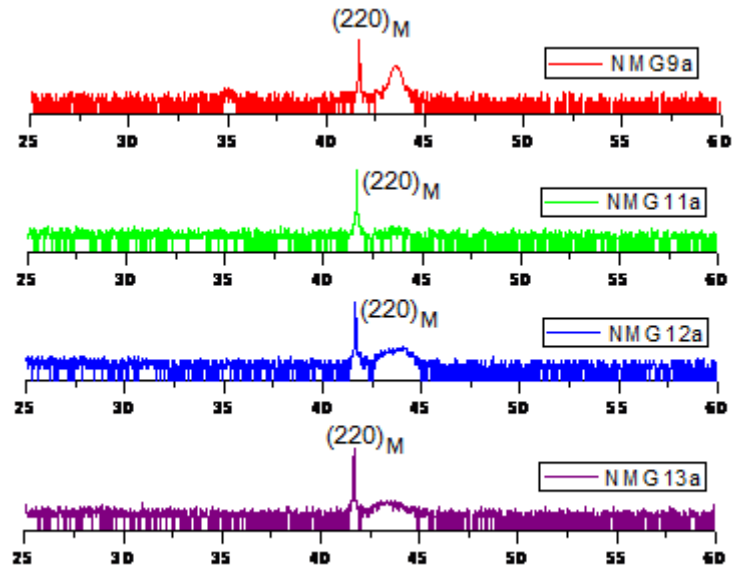


Fig. 4.24 XRD spectra for samples deposited on Al_2O_3 substrates

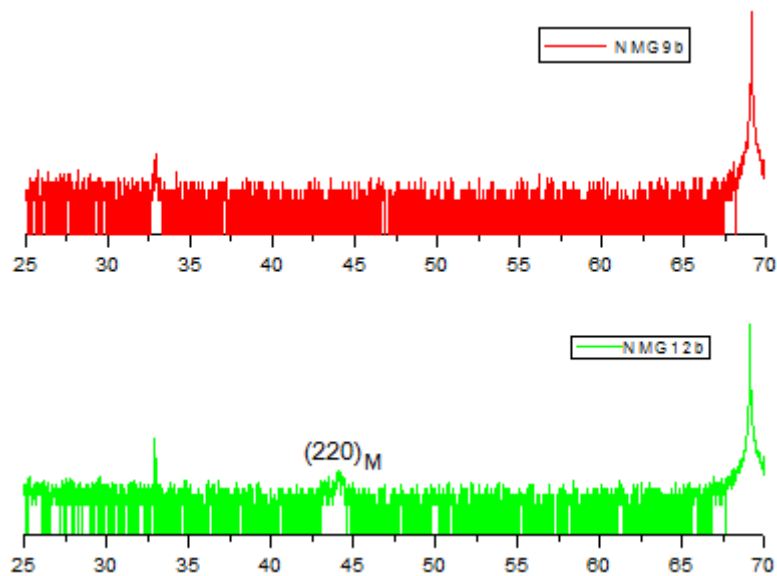


Fig.4.25 XRD spectra for samples deposited on Si substrates

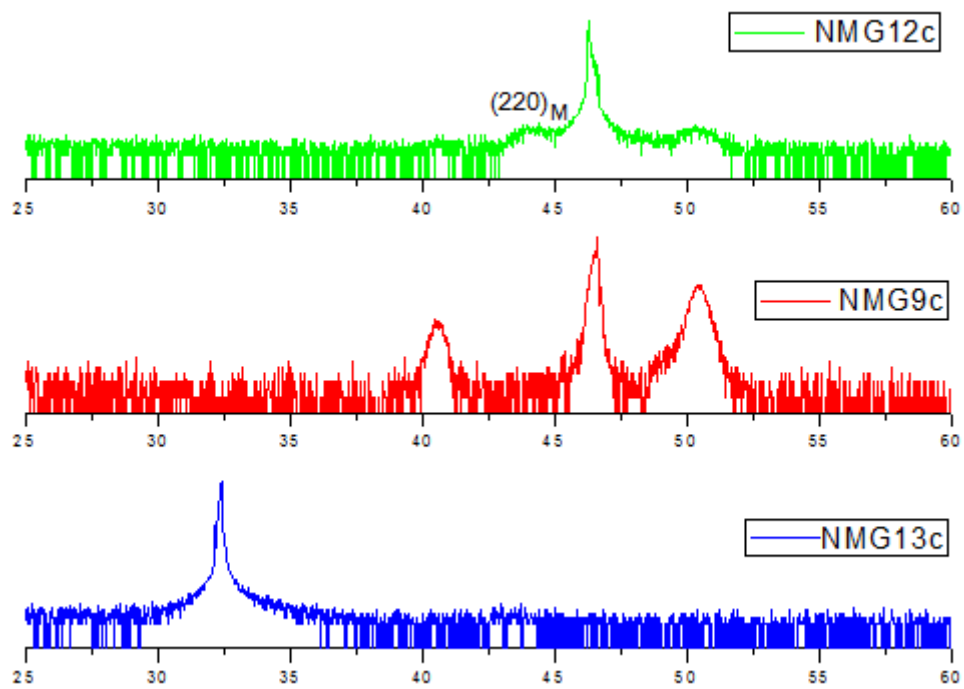


Fig. 4.26 XRD spectra for samples deposited on SrTiO₃ substrates

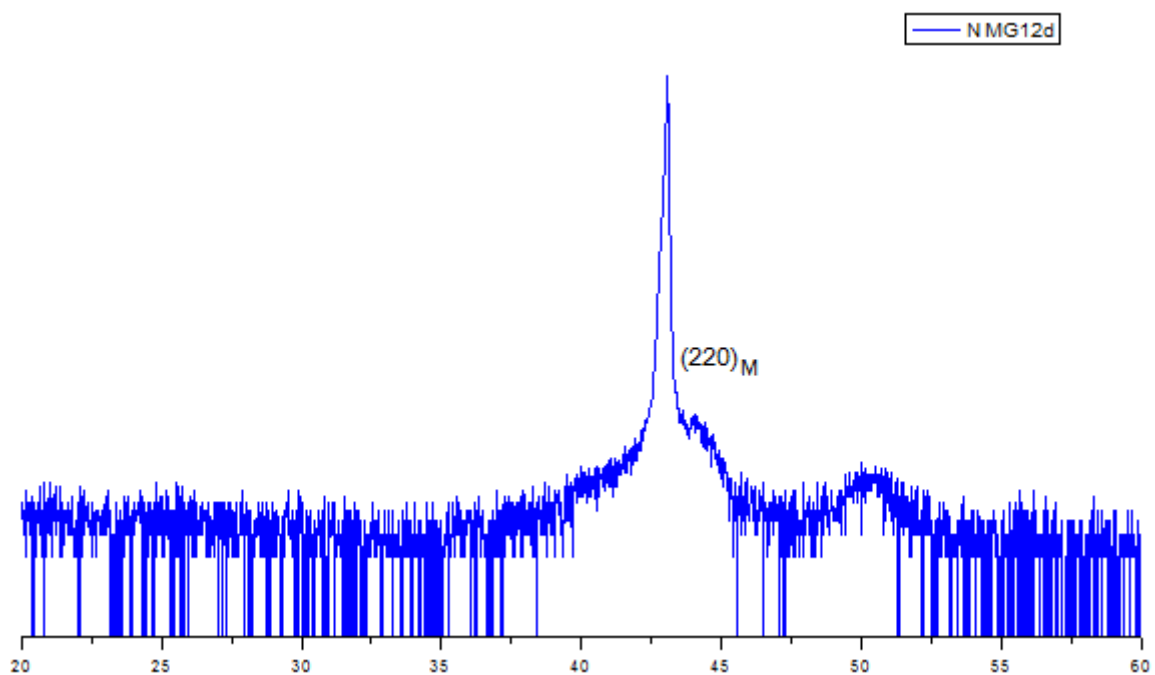


Fig. 4.27 XRD spectra for sample 12d, deposited on MgO substrate

From the analysis of the XRD spectra of the films we can only detect the existence of the martensitic phase, through the peak corresponding to the direction (220), and it is not visible for all the samples. This is the case of samples NMG9b, NMG9c, and NMG13c, which only show peaks from their substrates. The other samples show, more or less intensely, the (220) peak of the martensitic phase. The substrates' peaks on the diffraction pattern of each sample for which XRD measurements were made are listed on Table 4.3. Table 4.4 shows the angular position of the mentioned peak for each sample and the corresponding lattice parameter, calculated using the following formula:

$$a = \frac{\lambda \sqrt{(h^2+k^2+l^2)}}{2 \sin(\theta)} \quad (4.2)$$

where a is the lattice parameter of a cubic structure, λ is the wavelength of the CuK α radiation (1.5406 Å), θ is the angular position of the peak, and h, k and l are the Miller index of the considered plane.

Table 4.3 Substrate peaks for samples for which XRD measurements were made

SAMPLE	2 θ (°)	
NMG9a	41,8	
NMG11a	41,8	
NMG12a	41,8	
NMG13a	41,8	
NMG12b	32,5	69,0
NMG12c	46,5	51,0
NMG12d	42,5	50,0
NMG9b	32,5	69,0
NMG12b	32,5	69,0
NMG9c	46,5	51,0
NMG13c	32,5	

Table 4.4 Lattice parameter of the martensitic phase of several samples

SAMPLE	$\Theta(^{\circ})$	Lattice parameter (\AA)
NMG9a	21.75	5.88
NMG11a	21.90	5.84
NMG12a	22.00	5.82
NMG13a	21.80	5.87
NMG12b	21.95	5.83
NMG12c	22.00	5.82
NMG12d	22.00	5.82

The values found for the lattice parameter of the samples are in accordance with previous results [42][34]. The results obtained for samples NMG12c and NMG12d are the closest to the value of the lattice parameter of the bulk stoichiometric Ni_2MnGa , which is 5.81 \AA .

It is important to note that the performed XRD measurements were not HR-XRD (High Resolution X-ray Diffraction) measurements. HR-XRD would certainly show more peaks belonging to the films which would in turn allow a more accurate determination of the thin film's lattice parameter and a more complete phase identification.

4.4. MAGNETISATION MEASUREMENTS

Hysteresis loops of the magnetisation as a function of the applied field were systematically carried out for the samples at different temperatures. The curves show the magnetic moment per unit volume of the samples as a function of the applied magnetic field. The volume was determined from the thickness and area of the film used.

The substrates used to produce the samples are diamagnetic. This diamagnetic behaviour contributes to the magnetisation giving a negative contribution, linear in magnetic field. This translates on the existence of a slope on the magnetisation curve where it would otherwise be horizontal (in the absence of the diamagnetic contribution). For the accurate analysis of the dependence of the films' magnetisations on the applied field, it is necessary to remove the substrates' contributions to the magnetisation. This is easy to perform, since we only have to remove from the original data the value of the slope

observed. As an example, fig. 4.28 shows the results of magnetisation dependence on the magnetic field for the NMG8g sample before the removal of the diamagnetic contribution from the substrate, whereas fig. 4.29 shows the same results after the removal of the already mentioned contribution. The oscillations seen in both images are noise resulting from equipment limitations in terms of resolution.

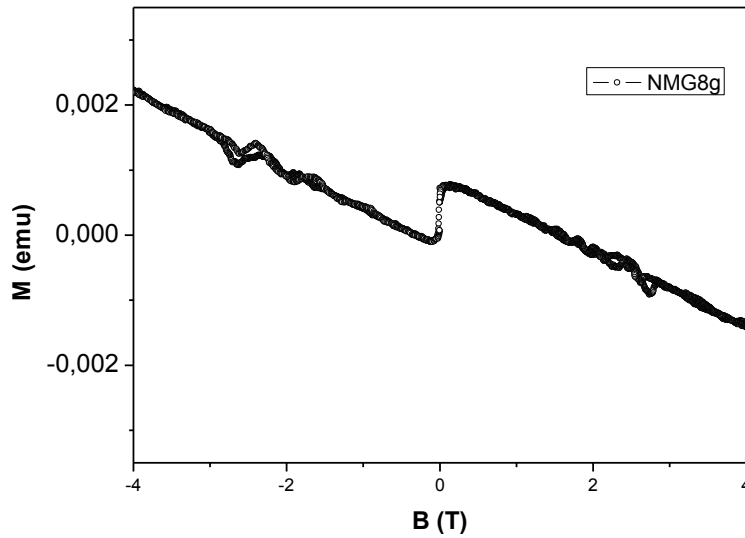


Fig. 4.28 *M-H loops carried out at for sample NMG8g before the removal of the substrate's contribution to magnetisation*

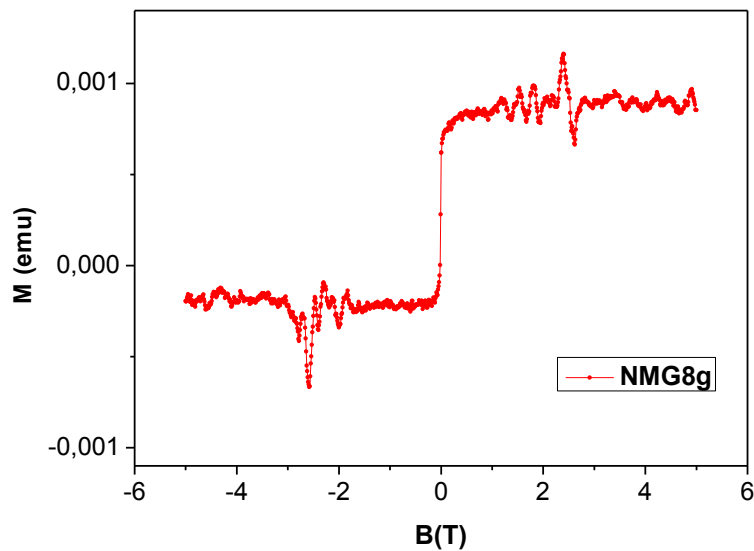


Fig. 4.29 *M-H loops carried out at for sample NMG8g after the removal of the substrate's contribution to magnetisation*

The obtained M-H loops will be presented in two different sets to allow a comparison between different characteristics of the samples. The first set of plots compares the M-H loops of samples deposited onto the same substrate, and which were taken at a given temperature. Thus, Figs. 4.30-33 show the M-H loops carried out at 150 K for samples deposited onto Al₂O₃, Si, SrTiO₃, and MgO substrates, respectively.

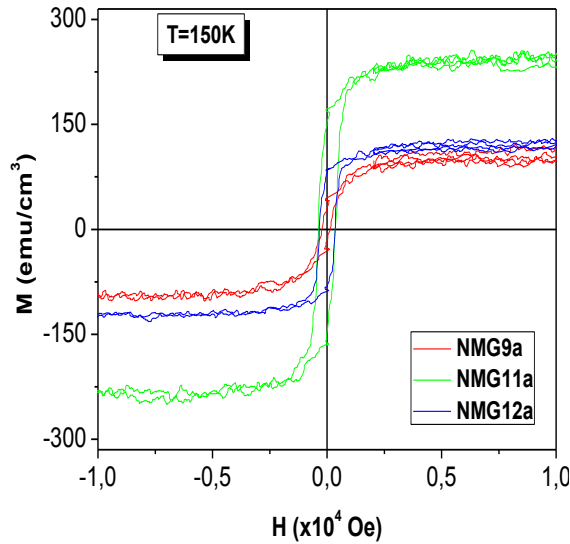


Fig. 4.30 M-H loops carried out at 150 K for samples deposited onto Al₂O₃ substrates

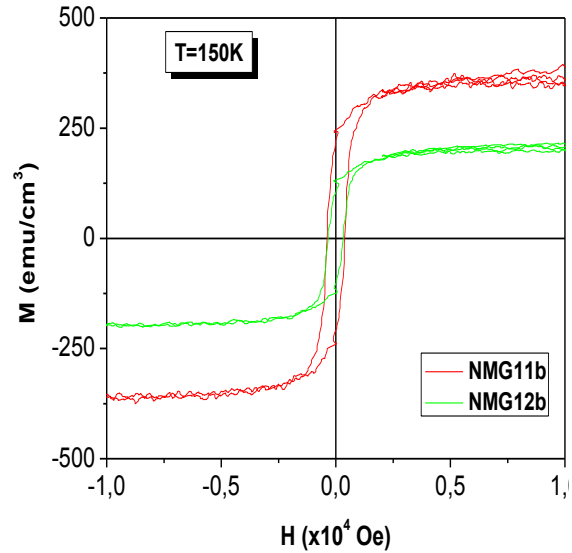


Fig. 4.31 M-H loops carried out at 150 K for samples deposited onto Si substrates

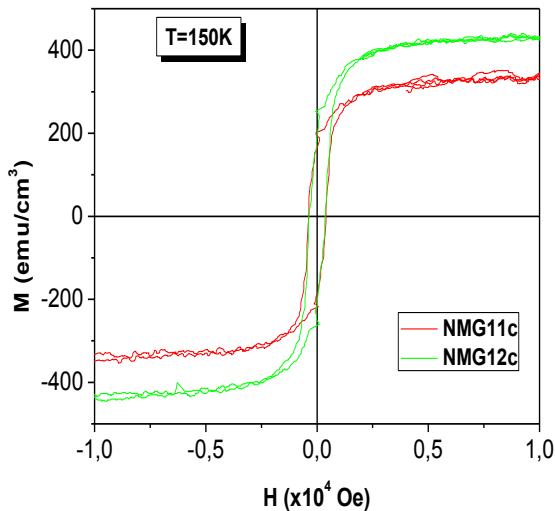


Fig. 4.32 M-H loops carried out at 150 K for samples deposited onto SrTiO₃ substrates

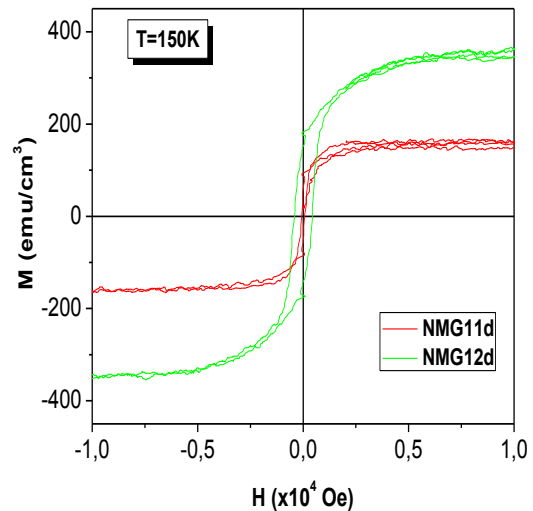


Fig. 4.33 M-H loops carried out at 150 K for samples deposited onto MgO substrates

Similarly, Figs. 4.34-37 show the M-H loops carried out at 300 K for samples deposited onto an Al_2O_3 , Si, SrTiO_3 , and MgO , respectively.

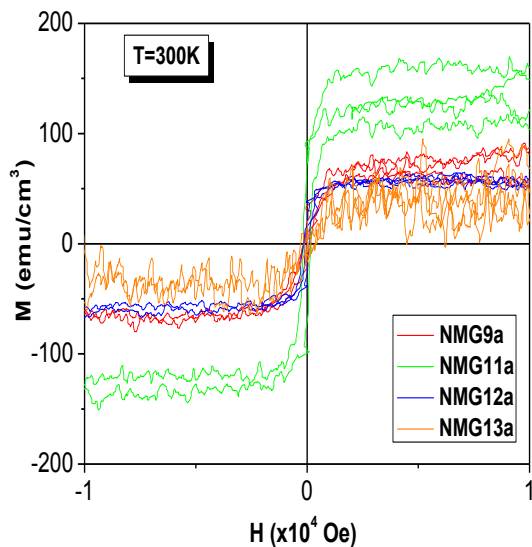


Fig. 4.34 M-H loops carried out at 300 K for samples deposited onto Al_2O_3 substrates

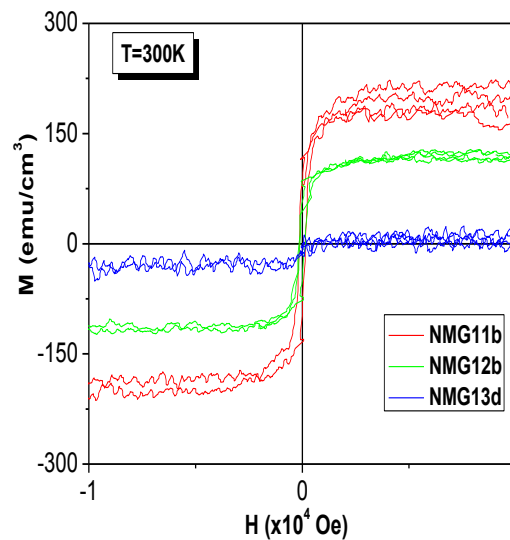


Fig. 4.35 M-H loops carried out at 300 K for samples deposited onto Si substrates

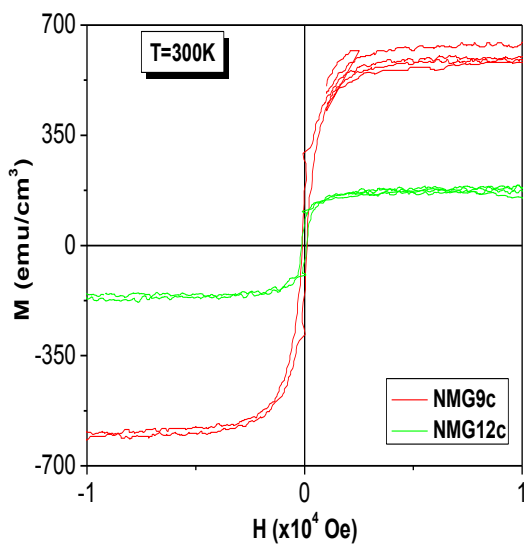


Fig. 4.36 M-H loops carried out at 300 K for samples deposited onto SrTiO_3 substrates

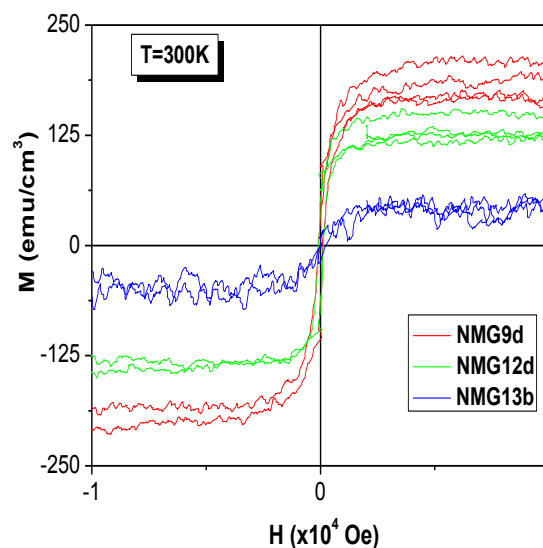


Fig. 4.37 M-H loops carried out at 300 K for samples deposited onto MgO substrates

The second set of plots compares the M-H loops of samples deposited onto different substrates under the same sputtering conditions, and which were taken at a given temperature. Thus, Figs. 4.38 and 4.39 show the M-H loops carried out at 150 K for samples of the series 11 and 12, respectively. Fig. 4.40 shows the M-H loops carried out at 100 K for samples of the series 13.

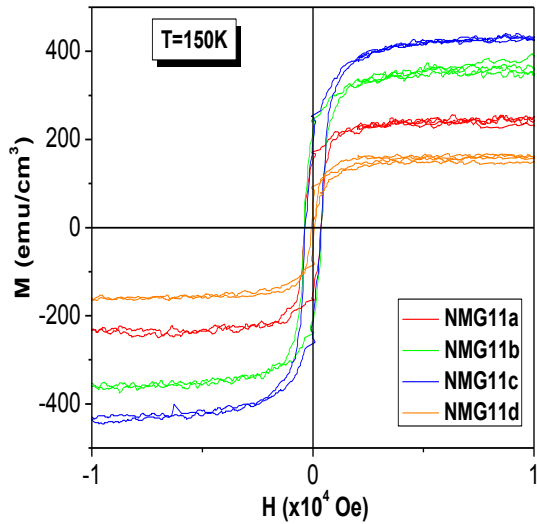


Fig. 4.38 M-H loops carried out at 150 K for samples of series 11 (same sputtering conditions)

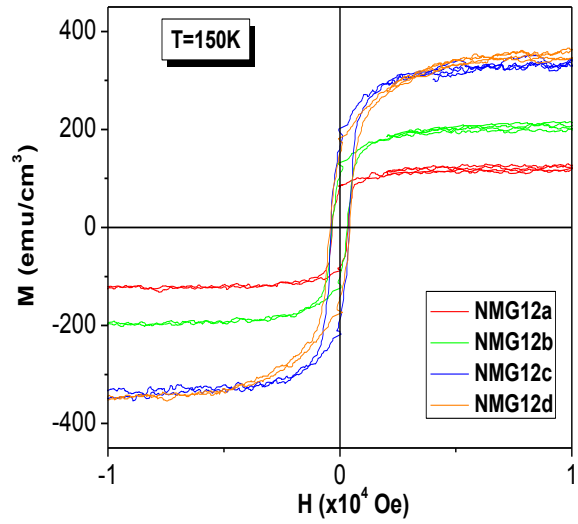


Fig. 4.39 M-H loops carried out at 150 K for samples of series 12 (same sputtering conditions)

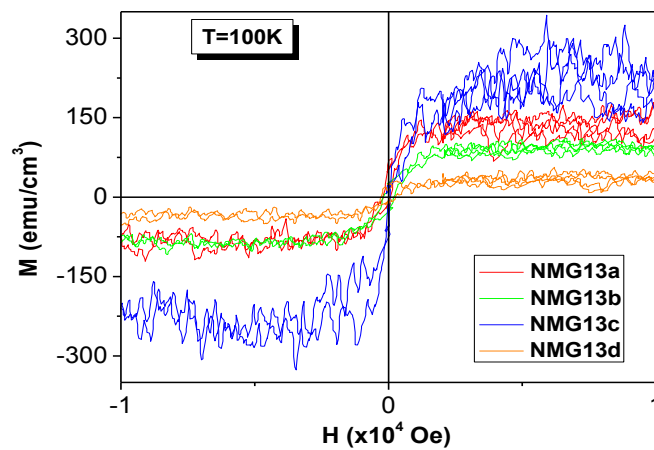


Fig. 4.40 M-H loops carried out at 100 K for samples of series 13 (same sputtering conditions)

Figs. 4.41-43 show the M-H loops carried out at 300 K for samples of the series 11 to 13, respectively. Fig. 4.44 shows the M-H loops carried out at 320 K for samples 11c and 11d. The measured saturation magnetization (M_S) and coercivity (H_C) are shown on Table 4.4.

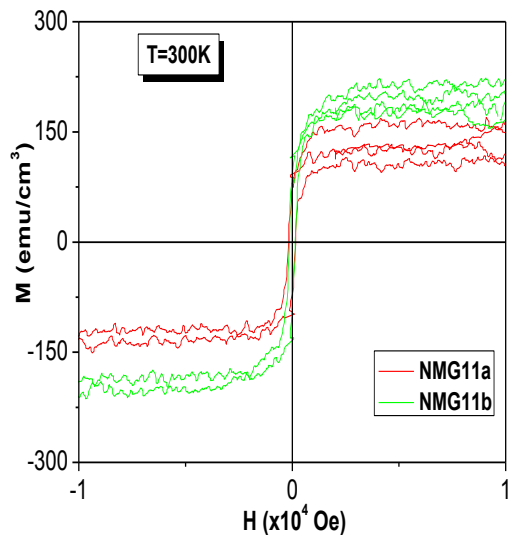


Fig. 4.41 M-H loops carried out at 300 K for samples of series 11 (same sputtering conditions)

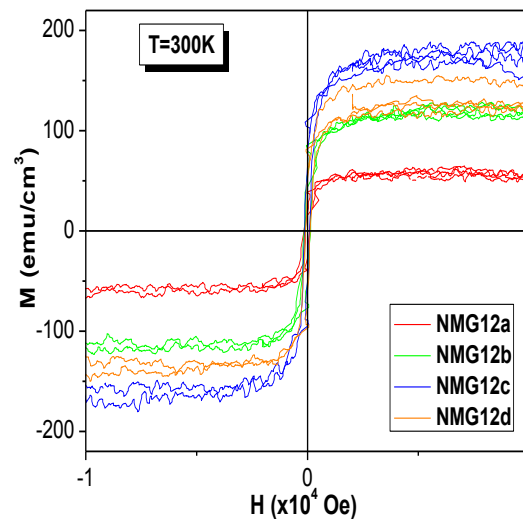


Fig. 4.42 M-H loops carried out at 300 K for samples of series 12 (same sputtering conditions)

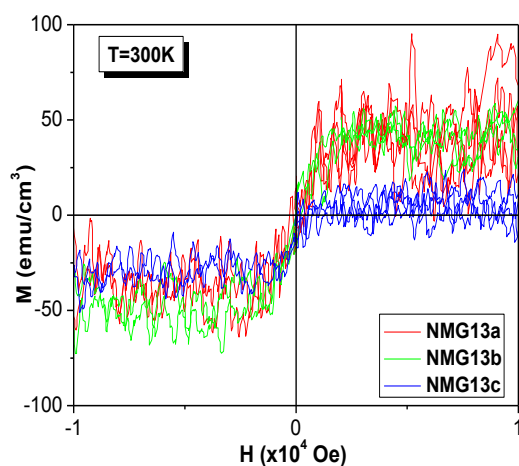


Fig. 4.43 M-H loops carried out at 300 K for samples of series 13 (same sputtering conditions)

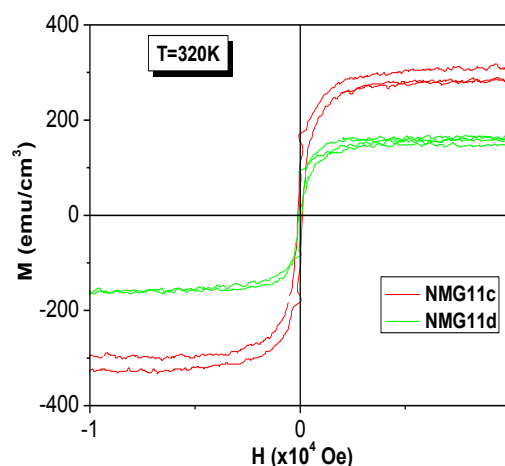


Fig. 4.44 M-H loops carried out at 320 K for samples of series 11 (same sputtering conditions)

Table 4.4 shows the most relevant features obtained from the M-H plots.

Saturation magnetisations of the measured films range from 30 emu/cm³ (observed for sample #13d at 300 K) to 600 emu/cm³ (observed for #9c sample at 300 K).

The values of the coercivity of the films go from 0.01x10⁴ Oe to 0.04x10⁴ Oe.

For an applied magnetic field of 0.5x10⁴ Oe all the samples have already attained saturation in magnetisation.

The coercivity of the samples belonging to series 9 have coercivity values approximately between 100 and 200 Oe. The coercivity of samples #9a and #9c does not depend on temperature. For this series of samples, saturation magnetisation increases for lower temperature. #9c (SrTiO₃ substrate) shows the strongest ferromagnetic signal.

For the samples of series 11, it is clear that the magnetic moment increases with decreasing measurement temperature. The coercivity of these samples varies between 100 Oe and 400 Oe and it increases with decreasing temperature. Sample #11c presents the highest values of magnetisation for this series.

Series 12 samples show a behaviour similar to that of series 11.

Series 13 samples would not present a relevant ferromagnetic signal due to their low thicknesses. For a density of sample of 8.16 g/cm³, the normalized saturation magnetization values at 150 K are: 1.1 μ_B/fu for sample NMG9a, 2.0 μ_B/fu for the samples of series 11, and 2.0 μ_B/fu for the samples of series 12. These results ensure high magnetic quality of the film, since the bulk magnetization value for the same composition, at 5K, is about 3 μ_B/fu (fig. 4.45) [43]. It is important to note that the saturation magnetisation of sample #9c at 300 K is significantly higher than those of the other samples in the same series. It is an atypical value that probably due to an experimental error.

Table 4.4 Values of saturation magnetisation (M_s) and coercivity (H_C) for several samples at different temperatures

SAMPLES	TEMPERATURE (K)	M_s (emu/cm ³)	H_C (x10 ⁴ Oe)
NMG9a	150	100	0.02
	300	80	0.02
NMG9c	300	600	0.01
NMG9d	300	190	0.01
NMG11a	150	230	0.03
	300	130	0.02
NMG11b	150	370	0.04
	300	220	0.01
NMG11c	150	300	0.04
	320	280	0.01
NMG11d	150	180	0.01
	320	150	0.01
NMG12a	150	120	0.03
	300	60	0.01
NMG12b	150	200	0.03
	300	110	0.02
NMG12c	150	400	0.04
	300	120	0.01
NMG12d	150	350	0.04
	300	125	0.01
NMG13a	100	130	-
	300	40	-
NMG13b	100	80	-
	300	50	-
NMG13c	100	230	-
	300	20	-
NMG13d	100	40	-
	300	30	-

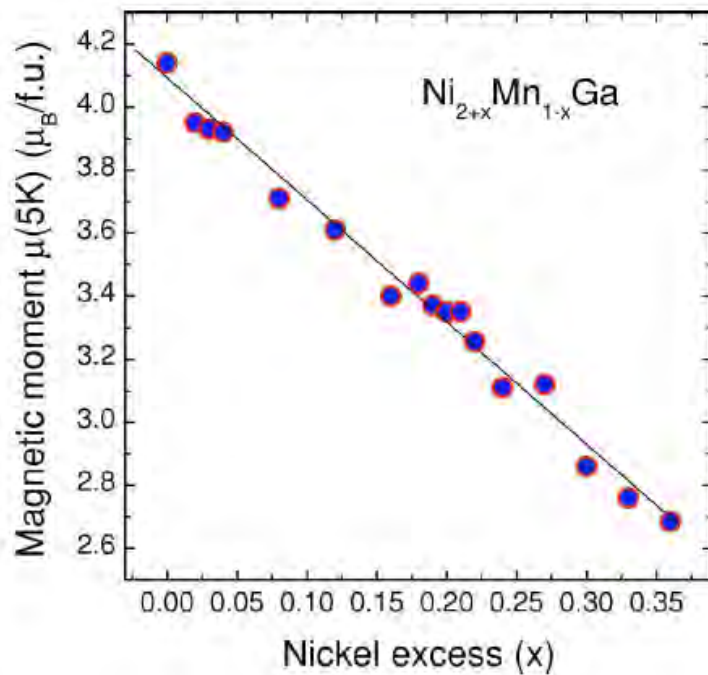


Fig. 4.45 Magnetic moment μ_B per formula unit as a function of Ni excess x in $Ni_{2+x}Mn_{1-x}Ga$ [43]

4.5. FERROMAGNETIC RESONANCE (FMR)

Ferromagnetic resonance is a special phenomenon characteristic of magnetic materials. The measurement of the ferromagnetic resonance has an important role in the study of such materials. FMR originates from the precessional motion of the magnetization of a ferromagnetic material in an external magnetic field H . The magnetic field operates a torque on the magnetization of the sample. This causes the magnetic moments in the sample to precess [25]. The presence of resonance allows to assess the orientation and magnitude of the magnetisation.

Ferromagnetic resonance measurements in the X-band (~ 9.47 GHz), in the temperature range from 280 K to 400 K, were performed for samples NMG12a (fig. 4.46) and NMG12b (fig. 4.47) by Prof. Nikolai A. Sobolev and Nuno M. Santos using the FMR Spectrometer of the Physics Department of the University of Aveiro.

These FMR measurements reveal, as expected [17], a Curie temperature (T_C) of approx. 350 K for both samples, which confirms the quality of the samples.

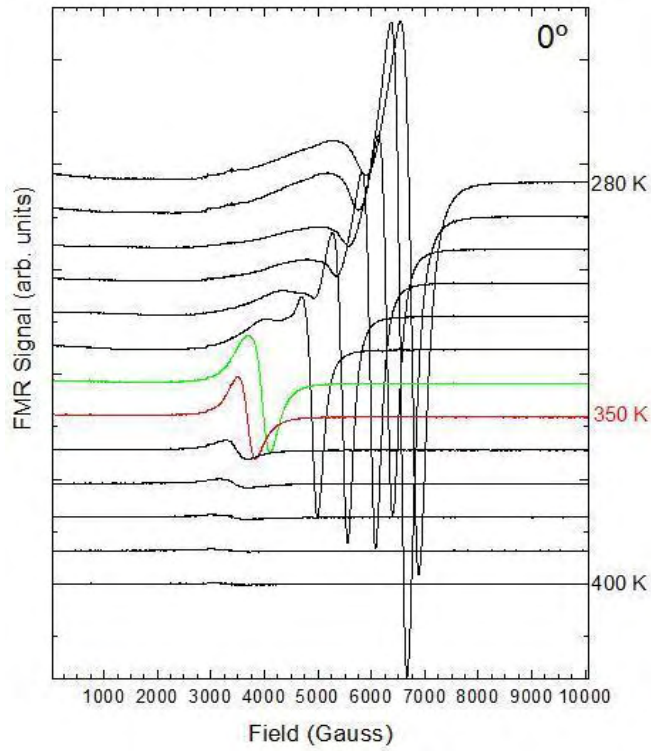


Fig. 4.46 FMR measurements carried out for several temperatures for sample NMG12a : $mwp = 2mW$, $Gain = 10^{-4}$, $F = 9.47 GHz$, standard cavity, out of plane, $T: 280-400K$, $\Delta T = 10K$, points: 2048.

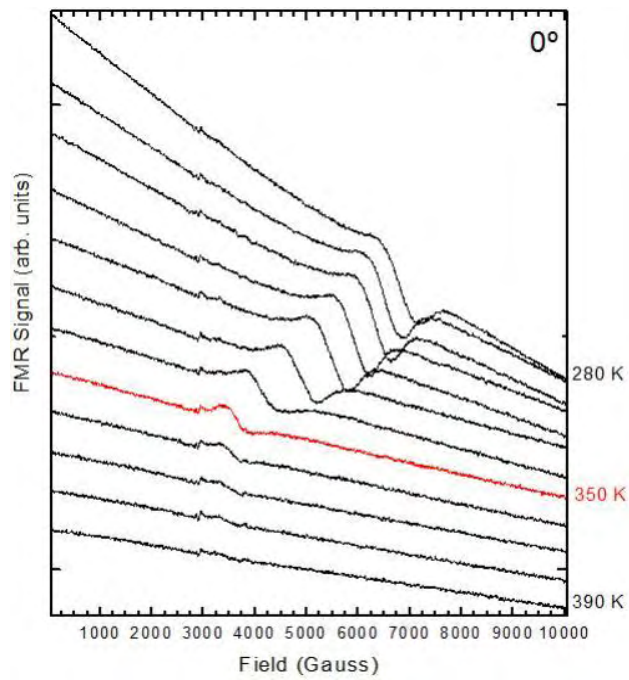


Fig. 4.47 FMR measurements carried out at different temperatures for sample NMG12b: $mwp = 2mW$, $Gain = 10^{-4}$, $F = 9.47 GHz$, standard cavity, out of plane, $T: 280-390K$, $\Delta T = 10K$, points: 2048.

5. CONCLUSIONS AND FUTURE STUDIES

5.1. CONCLUSIONS

The analysis of the composition of the several samples allowed us to conclude that increasing the sputtering power of each target will result in an increase of the percentage of the elements of that target on the deposited thin film. It was also observed that for some samples a change of substrate from Al_2O_3 to Si introduced a decrease in the percentage of Ni and an increase in the percentage of Mn. This change of substrate did not induce any change on the percentage of Ga. However, in the case of the same change in substrate, but this time for different samples (with different sputtering conditions from the previous), the percentage decreased for Mn and increased for Ga.

From the analysis of the XRD spectra of the films it was possible to detect only the existence of the martensitic phase, through the peak corresponding to the direction (220), and it wasn't observed in every sample. The values found for the lattice parameter of the samples for which the XRD was performed and where the (220) martensitic phase peak was observed presented an expected dependence on the film composition. HR-XRD (High Resolution X-ray Diffraction) measurements would certainly lead to the observation of more peaks belonging to the films which would in turn allow a more accurate determination of the thin film's lattice parameter and a more complete phase identification.

The measurements of magnetisation as a function of the applied field allowed us to conclude that most of the samples show saturation magnetisations of the same order of the saturation magnetisation of the bulk material of the same composition. It is also possible to safely state that the ferromagnetic behaviour of the thin films under study is stable up to 300K. The FMR measurements revealed for samples NMG12a and NMG12b, as expected [17], a Curie temperature (T_C) of approx. 350 K for both samples, which confirms their quality, since bulk T_C for the same composition is about 360K (figs. 2.1 and 4.45) [43].

The low temperature deposition (at around 400 °C) is successfully achieved. The samples show, at room temperature, high ferromagnetic signal. The values of the saturation magnetisation are high, approximately 70% of the saturation magnetisation of the bulk material with the same composition [43]. In fact, the normalized saturation magnetization values for a density of sample of 8.16 g/cm^3 are, at 150 K: $1.12 \mu_B/\text{fu}$ for sample NMG9a,

$2 \mu_B/\text{fu}$ for the samples of series 11, and $2 \mu_B/\text{fu}$ for the samples of series 12. These results ensure high magnetic quality of the film, since the bulk magnetization value for the same composition, at 5K, is $3 \mu_B/\text{fu}$ (figs. 2.1 and 4.45) [43].

5.2. FUTURE STUDIES

Since a good ferromagnetic signal was not obtained from samples of series 13 due to its very low thickness, all the magnetic measurements for this series are to be performed in SQUID.

Deposition of films on active substrates to analyse magneto-structural coupling is planned.

The temperature dependent magnetisation is to be studied with the goal of understanding T_c , structural transition and their history (temperature and magnetic field) dependence. Temperature dependence and hysteresis of the structural transformation are also to be studied.

Magnetic domain characterisation can be obtained with magnetic force microscopy (MFM). This will allow a better understanding of the relation between magnetic domain and mechanical domain.

It is also of interest to perform measurements of resistivity and magnetoresistance in order to characterise the electrical properties of the samples. It would also be interesting to study other Ni-Mn-Ga compositions.

6. BIBLIOGRAPHY

- [1] WASA K., KITABATAKE M. AND ADACHI H. *Thin Film Materials Technology: sputtering of compound materials*, William Andrew Publishing (2004)
- [2] OHRING M. *The materials science of thin films*, Academic Press (1991)
- [3] MAHAN J. *Physical Vapor Deposition of Thin Film*, Wiley-interscience (2000)
- [4] SESHAN K. *Handbook Of Thin Film Deposition Techniques Principles, Methods, Equipment And Applications, Second Editon* (2002)
- [5] MOSHFEGH A. Z., KANEL H. V., KASHYAP S. C. AND WUTTIG M. *Proceedings of the International Workshop on Physics and Technology of Thin Film*, World scientific pub. (2004)
- [6] MATTOX D. M. *The Foundations of Vacuum Coating Technology*, William Andrew Publishing (2003)
- [7] ROLF E., HUMMEL K., GUENTHER H. AND WISSMAN P., *Handbook of optical properties, volume 2*, Crc Press (1995)
- [8] SMITH D. L. *Thin-film deposition: principles and practice*, Mcgraw-hill Professional Publishing (1995)
- [9] LOGAN J. S. *IBM J. Res. Develop.*, 172-175 (1970)
- [10] WASER R. *Nanoelectronics and Information Technology: Advanced Electronic Materials and Novel*. Wiley-vch Verlag (2005)
- [11] SWANN S. *Phys. Technol.* **19**, 67 (1988)
- [12] PAOLETTI A. *The Physics of Diamond*, IOS Press (1997)
- [13] LEVY R. A. *Microelectronic materials and processes*, Kluwer Academic Publishers (1989)
- [14] MADOU M. J. *Fundamentals of microfabrication: The science of miniaturization*, Taylor & Francis (2002)
- [15] BEHRISCH R. *Sputtering by particle bombardment, Volume 1*, Springer (1991)
- [16] MATTOX D. M. *Handbook of Physical Vapor Deposition (PVD) Processing*, William Andrew Publishing (1998)
- [17] Planes A., Mañosa L., Saxena A. *Magnetism and structure in functional materials*, Springer Berlin Heidelberg (2006)

- [18] OHRING M. *The materials science of thin films: deposition and structure*, Academic Press (2001)
- [19] MARTON L. *Advances in Electronics and Electron Physics, Volumes 34-35*, Academic Press (1973)
- [20] FRIDMAN A. *Plasma Chemistry, Cambridge University Press* (2008)
- [21] SCHUEGRAF K. K. *Thin-Film Deposition Processes and Techniques*, William Andrew Inc. (1988)
- [22] BEHRISCH, R. *Topics in Applied Physics-Sputtering by Particle Bombardment I, 1st ed., Vol. 47*, Springer Verlag (1983)
- [23] DUCHEMIN O. B., BROPHY J. R., GARNER C. E., RAY P. K., SHUTTHANANDAN V. AND MANTENIEKS M. A. *A Review of Low Energy Sputtering Theory and Experiments*
- [24] WASA K., HAYAKAWA S. *Handbook of Sputter Deposition Technology: Principles, Technology and Applications*, Noyes Publications (1992)
- [25] Chen L., Varadan V., *Microwave electronics: measurement and materials characterization*, John Wiley & Sons (2004)
- [26] WELCH K. *Capture pumping technology*, North-Holland (2001)
- [27] MARTON L. *Advances in Electronics and Electron Physics*, Academic Press (1968)
- [28] AYUELA A., ENKOVAARA J., ULLAKKO K. AND NIEMINEN R. M. *J. Phys.: Condens. Matter* **11**, 2017–2026 (1999)
- [29] LESZCZYNSKI J. *Computational Materials science*, Elsevier Science & Technology (2004)
- [30] WEBSTER P.J., ZIEBECK K.R.A., TOWN S.L., PEAK M.S., *Philos. Mag. B* **49**, 295-310 (1984)
- [31] HONEYCOMBE R., BHADESHIA H. *Steels: microstructure and properties*, Butterworth-heinemann (1995)
- [32] RIGHI L., ALBERTINI F., CALESTANI G., PARETI L., PAOLUZI A., RITTER C., ALGARABEL P. A., MORELLON L. AND RICARDO I. M. *Journal of solid state chemistry* **11**, 3525-3533 (2006)
- [33] MURRAY V. N. *Progress in Ferromagnetism Research*, Nova Science Pub Inc (2006)
- [34] CHERNENKO V. A, LOPEZ A. R., KOHL M., BARANDIARAN J. M., OHTSUKA M., ORUE I. AND BESSEGHINI S. *Acta materialia* **20**,5461-5467 (2006)

- [35] KOKORIN V.V., CHERNENKO V.A., VAL'KOV V.I., KONOPLYUK S.M., E.A. KHAPALYUK, *Phys. Solid State* **37**, 2049 (1995)
- [36] GONZÁLEZ-COMAS A., OBRADÓ E., MAÑOSA L., PLANES A., CHERNENKO V. A., HATTINK B.J. AND LABARTA A., *Phys. Rev. B* **60**, 7085 (1999).
- [37] ZHANG Z.Y., DU Z.W., SHAO B.L., LIU A.S. AND SUN Z.M. *Materials Characterization* **8**, 1041-1045 (2008)
- [38] BERNARD F., DELOBELLE P., ROUSSELOT C. AND HIRSINGER L. *Thin solid films pre-publication* (2009)
- [39] CHEETHAM A., DAY P. *Solid state chemistry: techniques*, Oxford University Press (1988)
- [40] PLANES A., MANOSA L. *International Conference on Advanced Structural Functional Materials Design 2008 Journal of Physics: Conference Series* **165** (2009)
- [41] EHRENREICH H., SPAEPEN F., *Solid state physics*, Academic Press (2004)
- [42] ANNADURAI A, NANDAKUMAR A. K., JAYAKUMAR S., KANNAN M.D., MANIVEL RAJA M., BYSAK S., GOPALAN R., CHANDRASEKARAN V. *Journal of Magnetism and Magnetic Materials* **321**, 630–634 (2009)
- [43] V. V. KHOVAYLO V. V., BUCHELNIKOV V. D., KAINUMA R., KOLEDON V. V., OHTSUKA M., SHAVROV V. G., TAKAGI T., TASKAEV S. V., VASILIEV A. N. *Physical Review B* **72**, 224408/1-224408/10 (2005)
- [44] O'HANDLEY R. C., MURRAY S. J., MARIONI M., NEMBACH H., ALLEN S. M. *Journal of applied physics* **87**, 4712-4716 (2000)